

# Conditional sampling of transitional boundary layers in pressure gradients

Kevin P. Nolan and Tamer A. Zaki†

Department of Mechanical Engineering, Imperial College, London SW7 2AZ, UK

(Received 17 July 2012; revised 20 January 2013; accepted 1 June 2013;  
first published online 9 July 2013)

Statistical analysis of transitional boundary layers in pressure gradients is performed using the flow fields from direct numerical simulations of bypass transition. Laminar–turbulent discrimination separates the streaky laminar flow from turbulent regions. Individual streaks are identified and tracked in the flow field in order to obtain statistics of the amplitude of the streak population. An extreme value model is proposed for the distribution of streak amplitudes. It is also possible to differentiate those streaks which break down into turbulent spots from innocuous events. It is shown that turbulence onset is due to high-amplitude streaks, with streamwise perturbation velocity exceeding 20% of the free stream speed. The resulting turbulent spots are tracked downstream. The current analysis allows for the measurement of the lateral spreading angles of individual spots and their spatial extent and volumes. It is demonstrated that the volumetric growth rate of turbulent spots is insensitive to pressure gradient.

**Key words:** boundary layers, instability, transition to turbulence

---

## 1. Introduction

Boundary-layer transition to turbulence is often described in terms of the initial amplification of a primary instability wave, a secondary instability and ultimately nonlinear breakdown into localized turbulent spots. This description originally emerged for the study of orderly transition, where the primary stage is the amplification of classical Tollmien–Schlichting (TS) waves (Kleiser & Zang 1991). A similar view has emerged for bypass transition, which takes place in the presence of appreciable background disturbances (Durbin & Wu 2007). In this case, the primary disturbances are elongated boundary-layer streaks, which reach high amplitude prior to their secondary instability. While the transitional boundary layer is laden with streaks, only a few undergo a localized secondary instability, which subsequently develops into a turbulent spot. The turbulent spots spread as they convect downstream and merge, thus forming a fully turbulent boundary layer. The sporadic and localized nature of transition onset is both intriguing and challenging to study.

In this work, direct numerical simulations (DNS) of bypass transition are performed for four different pressure gradients. Conditional sampling of the spatially and temporally resolved flow fields is performed in order to determine the distribution of streak amplitude as well as the threshold for emergence of turbulent spots. The

† Email address for correspondence: [t.zaki@imperial.ac.uk](mailto:t.zaki@imperial.ac.uk)

ensuing turbulent spots are also tracked in space and time, and their growth rates contrasted under different pressure gradients.

### 1.1. Klebanoff streaks

Streaks are ubiquitous features of boundary layers subject to elevated levels of free stream turbulence. They were originally described as breathing modes, because they are accompanied by thickening and thinning of the instantaneous boundary-layer edge (Klebanoff 1971), and were later termed Klebanoff modes by Kendall (1991). These low-frequency perturbations extend the length of the pre-transitional boundary layer, and are characterized by their high-amplitude streamwise velocity disturbance,  $u'$  (Jacobs & Durbin 2001). An important measure of a streak intensity is its amplitude  $A_u$ , which is the local maximum in the  $u$  perturbation profile. In the cross-flow plane, the streak size is of the order of the boundary-layer thickness in both span and height. The mechanism for the generation and amplification of boundary-layer streaks has received a great deal of attention in the literature (Taylor 1923; Landahl 1975; Goldstein & Wundrow 1998; Matsubara & Alfredsson 2001).

Many of the characteristics of boundary-layer streaks have been explained using linear analysis. Rapid distortion theory explains their long streamwise extent (Phillips 1969). The analysis of Hultgren & Gustavsson (1981) shows linear growth of the disturbance amplitude in time, and its subsequent decay due to viscous dissipation. Andersson, Berggren & Henningson (1999) computed the optimal streak disturbance in a spatial boundary layer. Their analysis predicts the experimentally observed spanwise spacing of the streaks. They also showed linear spatial amplification of streak amplitude, which is also consistent with experiments. Zaki & Durbin (2006) investigated the influence of pressure gradient. Using linear analysis and DNS, they demonstrated that adverse (favourable) pressure gradient enhances (reduces) the amplitude of the streaks, and hence promotes (delays) transition to turbulence. In addition, linear analyses were also performed to predict the threshold of the streak secondary instability (Vaughan & Zaki 2011).

Streaks are observed to be complicit in the accelerated breakdown to turbulence in bypass transition (e.g. the flow visualizations by Matsubara & Alfredsson (2001) and Mans *et al.* (2005)). Their role has been empirically described based on DNS of transition in flat-plate boundary layers (Jacobs & Durbin 2001; Liu, Zaki & Durbin 2008a), downstream of different leading-edge geometries (Nagarajan, Lele & Ferziger 2007), and in more complex flow configurations such as compressor passages (Zaki *et al.* 2009). One principal breakdown mechanism is the secondary instability of lifted low-speed streaks, when they are buffeted by the high-frequency, free stream disturbances (Jacobs & Durbin 2001; Zaki & Durbin 2005). The simulations of Nagarajan *et al.* (2007) also predicted transition onset near the edge of the boundary layer when the leading-edge geometry was slender. However, a blunt leading edge yielded a new breakdown mechanism via near-wall wavepackets.

In analogy to the work of Swearingen & Blackwelder (1987) on Görtler vortices, secondary instability analysis has been applied to streaky boundary layers (e.g. Andersson *et al.* 2001; Liu, Zaki & Durbin 2008b). Recently, Vaughan & Zaki (2011) were able to explain the empirical observations of Nagarajan *et al.* (2007). Their secondary instability analysis predicted two modes of instability. The first is an outer mode that causes breakdown of the lifted streaks near the edge of the boundary layer. The second mode is an 'inner instability' that leads to the formation of wavepackets, which precede full nonlinear breakdown to turbulence.

It is clear from both experimental and numerical studies that not all streaks undergo secondary instability and breakdown to turbulence. In fact, the majority of streaks are innocuous. Time-averaged statistics such as the root mean square velocity (r.m.s.) are frequently cited as an indication of streak intensity. However, such statistics mask the distribution of streak amplitudes in transitional boundary layers, and the rare, unique events that lead to breakdown to turbulence. This point was highlighted by the experiments of Hernon, Walsh & McEligot (2007) and Nolan, Walsh & McEligot (2010), who reported peak amplitudes of greater than 30% of the free stream velocity.

In this work we examine the population of streaks from DNS databases of bypass transition in a pressure gradient. Individual streaks are identified and tracked in space and time. The evolution of a particular streak can thus be treated as a single event and statistics of the population of these events evaluated.

### 1.2. *Turbulent spots*

Emmons (1951) coined the term ‘turbulent spot’ and proposed the concept of intermittency to describe the flow as it locally switches between laminar and turbulent states. Beyond their initial local inception, spots rapidly grow in size as they convect downstream. The intermittency factor therefore increases from zero in the pre-transitional region where there is no turbulence to unity as the flow becomes increasingly turbulent, culminating in a fully turbulent boundary layer. Emmons supposed a conical growth of a two-dimensional spot in time and proposed a spot spreading angle from the point of inception to the spanwise tips of the growing structure.

Schubauer & Klebanoff (1955) used a spark-generating apparatus to repeatedly trigger ‘artificial’ turbulent spots in a Blasius boundary layer for interrogation using hot-wire anemometry. The flow visualization by Gad-El-Hak, Blackwelder & Riley (1981) clearly identified the leading-edge overhang, the trailing-edge ‘calmed’ region and the distinctive arrowhead shape of the turbulent spots. Cantwell, Coles & Dimotakis (1978) applied a conical transformation to measurements of artificial spots and demonstrated the similarity of the spot-structure during its evolution. Further experiments on artificial spots have considered the effects of pressure gradient on spot growth and spreading angle (Wynanski, Sokolov & Friedman 1976; Seifert & Wynanski 1995). Since much of the work on artificial spots is based on a disturbance introduced at the wall, Jacobs & Durbin (2001) remarked that there may be a difference in the structure of ‘top-down’ versus ‘bottom-up’ spots, since their reported breakdown mechanism is found to occur at the edge of the boundary layer and not at the wall.

Other researchers have probed turbulent spot structure and growth by measuring spots evolving naturally in boundary layers using laminar–turbulent discrimination techniques (Hedley & Keffer 1974; Volino & Pratt 2003). The flow is separated into its constituent laminar and turbulent components and the statistics for each considered separately. Dhawan & Narasimha (1958) showed that several boundary-layer parameters may be obtained by the linear combination of their laminar and turbulent components weighted on the local Emmons intermittency factor. Ching & LaGraff (1995) measured the propagation rates of naturally occurring spots under moderate levels of free stream turbulence and found similar leading- and trailing-edge velocities as those reported for artificially generated spots. Anthony, Jones & LaGraff (2005) employed a novel experimental technique using hot-film arrays to image the surface heat flux on a flat plate subject to free stream turbulence. Similarities with the simulations of Jacobs & Durbin (2001) were reported. Abu-Ghannam & Shaw (1980)

investigated the effect of pressure gradient on bypass transition. They demonstrated that, with increasingly favourable pressure gradient, transition onset is delayed and the length of the transition region extended. Most recently, Park *et al.* (2012) highlighted the similarity in the flow statistics within the turbulent patches, which they identified using an enstrophy-based criterion, and fully turbulent boundary layers.

Using laminar–turbulent discrimination techniques, herein we identify the inception location of turbulent spots in the DNS database of bypass transition. Furthermore, we evaluate the growth rates of individual turbulent spots in the simulations and examine the influence of pressure gradient.

## 2. Direct numerical simulations

DNS of boundary-layer transition beneath free stream turbulence were performed for four pressure gradient conditions. The details of the numerical algorithm and the set-up of the simulations are described in this section. The Navier–Stokes equations were discretized on a curvilinear staggered grid using the local volume flux formulation (Rosenfeld, Kwak & Vinokur 1991; Wu & Durbin 2001). A fractional step procedure was used to advance a provisional velocity field, which was projected onto the divergence-free solution using the updated pressure. The convective terms were advanced using the Adams–Bashforth method; the pressure and diffusive terms were treated using implicit Euler and Crank–Nicolson scheme, respectively. The algorithm has previously been used in a number of studies of breakdown to turbulence, including simulations of bypass transition in pressure gradients, separation-induced transition and breakdown due to Görtler instability (Zaki *et al.* 2010; Schrader, Brandt & Zaki 2011).

The computational set-up is similar to the DNS of bypass transition by Jacobs & Durbin (2001). The parameters of the current simulations are summarized in table 1. (The four simulation cases represent favourable, zero, adverse and strongly adverse pressure gradient, and are hereafter referred to as *FPG*, *ZPG*, *APG* and *APG<sub>strong</sub>*, respectively.) The flow domain starts at  $x = x_0$ , which is located downstream of the leading edge. At the inlet, the Reynolds number is  $Re \equiv U_\infty \delta_0 / \nu = 800$  based on the inflow free stream velocity  $U_\infty$ , the 99% boundary-layer thickness  $\delta_0 = \delta(x = x_0)$  and the kinematic viscosity  $\nu$ . All subsequent results are normalized by  $U_\infty$  and  $\delta_0$  unless otherwise stated. The domain height at the inlet is  $L_y = 40$  and the spanwise size is  $L_z = 30$ . The streamwise extent was chosen such that transition was complete within the computational domain. Therefore, a relatively short domain length was sufficient for the adverse pressure conditions,  $L_x = 600$ , while longer domains were required for the zero and favourable pressure gradient simulations,  $L_x = 900$  and  $1200$ , respectively. The grid resolution was based on the final simulations by Jacobs & Durbin (2001), who performed a detailed grid refinement study. The grid spacing is uniform in the streamwise and spanwise directions, where a finer resolution is adopted in the current work. In the wall-normal direction, the grid was clustered inside the boundary layer using a hyperbolic tangent function, with the cell size at the wall  $\Delta y_w^+ \equiv \Delta y_w u_\tau / \nu < 0.40$ , where  $u_\tau$  is the friction velocity.

The top boundary of the computational domain is contoured in order to provide a desired streamwise pressure gradient. The top boundary condition is free-slip, similar to the work by Zaki & Durbin (2006). Four different free stream acceleration parameters  $\beta$  were simulated, where  $U_\infty(x) = Kx^{\beta/(2-\beta)}$ . These can be directly related to the pressure gradient parameter  $\lambda_\theta \equiv (\theta^2/\nu) dU_\infty/dx$ , where  $\theta$  is the momentum thickness. The resulting streamwise development of the free stream velocity,  $U_\infty(x)$ ,

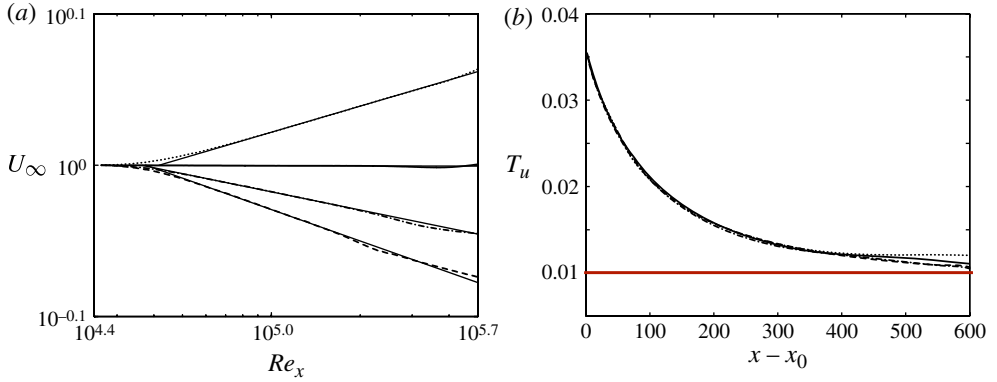


FIGURE 1. (a) Streamwise development of free-stream velocity,  $U_\infty$ , and (b) decay of turbulence intensity for each case: *FPG* (dotted); *ZPG* (solid); *APG* (dash-dotted); *APG<sub>strong</sub>* (dashed).

| Case                        | $\lambda_\theta$ | $\beta$ | $L_x$ | $n_x \times n_y \times n_z$  | $dt$    |
|-----------------------------|------------------|---------|-------|------------------------------|---------|
| <i>APG<sub>strong</sub></i> | -0.04            | -0.14   | 600   | $2048 \times 192 \times 192$ | 0.05    |
| <i>APG</i>                  | -0.02            | -0.08   | 600   | $2048 \times 192 \times 192$ | 0.05    |
| <i>ZPG</i>                  | 0                | 0       | 900   | $3072 \times 192 \times 192$ | 0.05    |
| <i>FPG</i>                  | 0.02             | 0.11    | 1200  | $4096 \times 192 \times 192$ | 0.03125 |

TABLE 1. Summary of simulation parameters, respectively, pressure gradient design parameter, Falkner–Skan parameter, domain length, grid size, and simulation time step.

is shown in figure 1. The slopes of the fitted lines match the design values for  $\beta$  (table 1).

The inflow condition is identical among all the simulations presented herein. It is a superposition of a Blasius mean velocity profile and free stream turbulence with an intensity of  $T_u = 3\%$ . The free stream turbulence is synthesized from Fourier modes in time and the periodic spanwise direction, and Orr–Sommerfeld and Squire modes in the wall-normal direction, as described by Jacobs & Durbin (2001) and Brandt, Schlatter & Henningson (2004). A von Kármán energy spectrum is assumed for the free stream turbulence condition,

$$E(\kappa) = T_u^2 E_0(\kappa) = T_u^2 \frac{(\kappa L)^4}{C[1 + (\kappa L)^2]^{17/6}}, \quad (2.1)$$

where  $\kappa$  is the length of the three-dimensional wavenumber vector,  $\kappa = \sqrt{k_x^2 + k_y^2 + k_z^2}$ . The expressions for  $C$  and  $L$  were given by Jacobs & Durbin (2001). The normalization constant  $C$  is determined by ensuring that  $\int_0^\infty E_0(\kappa) d\kappa = 3/2$ , and the turbulence length scale  $L$  is given by  $L = 55C/9\pi L_{11}$ , where  $L_{11}$  is given by  $L_{11} \equiv (1/T_u^2) \int_0^\infty [u(x)u(x+r)] dr$ . The downstream decay of free stream turbulence intensity is plotted in figure 1 for each pressure gradient case.

For each flow condition, the initial transient was removed and statistics were collected during approximately 8000 time units. This period corresponds to a

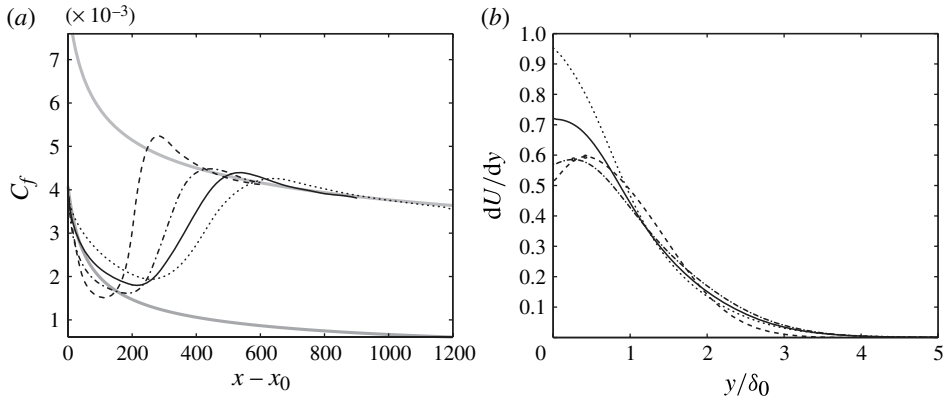


FIGURE 2. (a) Skin friction, normalized by local free-stream velocity, for all cases: *FPG* (dotted); *ZPG* (solid); *APG* (dash-dotted); *APG<sub>strong</sub>* (dashed); laminar and turbulent  $C_f$  predictions for zero pressure gradient (grey). (b) First derivative of the mean velocity profile at the streamwise location where  $C_f$  is minimum. A circle marks the wall-normal location of the inflection point in the velocity profile for the adverse pressure gradient cases.

non-dimensional frequency,  $F \equiv (\omega v/U_\infty^2) \times 10^6 \approx 1$ . For comparison, the lowest disturbance frequency at the inflow was  $F \approx 228$ . Spanwise- and time-averaged statistics were computed during the simulations. In addition, a database of 4000 subdomain snapshots comprising every other point of the velocity field was created for further analysis. Snapshots were separated by two convective time units. Throughout the results, upper-case symbols or an overbar denote mean quantities, and the prime denotes perturbation quantities, for example  $\mathbf{u}' = \mathbf{u} - \mathbf{U}$ .

The average skin friction for each case is plotted in figure 2 versus streamwise distance,  $x - x_0$ , where  $x_0$  is the domain inlet. Also shown are predictions for laminar and turbulent flow given by  $C_{f,LAM} = 0.664/Re_x^{0.5}$  and  $C_{f,TURB} = 0.455/\ln^2(0.06Re_x)$ . The skin friction is fixed by the inflow Blasius profile and then adjusts according to the downstream pressure gradient. Transition onset is indicated by the skin friction minimum, and downstream  $C_f$  steadily approaches the higher turbulent level where the boundary layer becomes fully turbulent. Transition is early and abrupt for the strong adverse pressure gradient, but occurs further downstream and is longer with the increasingly favourable flows. The adverse pressure gradient velocity profiles are inflectional at transition onset as indicated on the right side of figure 2.

The maximum of  $u_{rms}$  in the wall-normal direction, figure 3, shows similar variation with pressure gradient. For all cases, a rapid increase is observed in the pre-transitional region, i.e. prior to the minimum in skin friction, which represents the growing amplitude of the boundary-layer streaks. This initial growth is followed by a ‘shoulder’ region where the growth rate slows before a significant secondary growth and peak in the middle of the transition region, corresponding to where the skin friction is midway between laminar and turbulent states. As the skin friction approaches the turbulent level, the data in figure 3 collapse to a consistent level of about 12%. The initial linear growth and streamwise peak show a dependence on pressure gradient. The curves, however, collapse in the pre-transitional region when plotted against  $Re_\theta$ . The wall-normal position of maximum  $u_{rms}$  is also shown in figure 3. It approaches the wall monotonically from the inlet until transition onset, thereafter levelling off at the same level for all cases, consistent with a turbulent boundary layer.

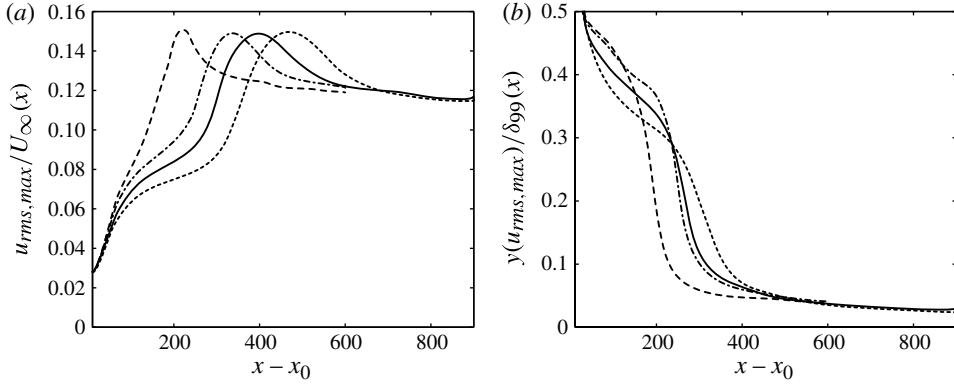


FIGURE 3. (a) Maximum of  $u_{rms}$  in the wall-normal direction normalized by the local free-stream velocity,  $U_\infty(x)$ , for all cases: *FPG* (dotted); *ZPG* (solid); *APG* (dash-dotted); *APG<sub>strong</sub>* (dashed). (b) Wall normal location of maximum  $u_{rms}$ .

### 3. Conditional sampling

Typically, statistics gathered from transitional flows contain contributions from both laminar streaks and turbulent spots, such as the peak  $u_{rms}$  distributions in figure 3. Conditional sampling of the flow fields can be used to separate turbulent regions from the streaky laminar flow. This allows the growth and subsequent decay of the streaks to be measured independently. In addition, turbulence statistics within the turbulent spots may be collected. The pronounced peak in  $u_{rms}$  in figure 3 and the overshoot in skin friction towards the end of transition suggest that fluctuations in turbulent spots are more energetic than typically found in fully turbulent flows. Statistics of spot propagation speed and growth rate may also be evaluated for comparison with the literature.

#### 3.1. Laminar–turbulent discrimination

The laminar–turbulent discrimination technique used herein is adapted from the methods discussed by Hedley & Keffer (1974). These typically involve the careful thresholding of an input signal, such as a time trace from a hot-wire probe, to identify turbulent regions. Often some form of sensitization is required to prepare the signal for accurate discrimination such as the time derivative. The resulting detector function is then lowpass-filtered and thresholded to obtain an indicator function, a logical indicator of laminar or turbulent flow, which is zero for laminar flow and unity for turbulent flow.

For the DNS flow fields, laminar–turbulent discrimination is applied to each snapshot independently. Since streaks are predominantly confined to the streamwise velocity component, and turbulence is manifest by significant fluctuation in all velocity components, a suitable detector function is the sum of the absolute values of the wall-normal  $v'$  and spanwise  $w'$  fluctuation fields,  $D \equiv |v'| + |w'|$ . The detector function is sensitized and lowpass-filtered in three-dimensional space by a local standard deviation filter. The logical indicator function,  $\Gamma$ , is obtained by thresholding the filtered signal at each wall-normal location using Otsu’s method (Otsu 1979) – a common technique in machine vision and image analysis for efficient thresholding of bimodal inputs. A common challenge in conditional sampling is robust threshold selection. Otsu’s method identifies the optimum threshold suggested by Hedley & Keffer (1974) by minimizing

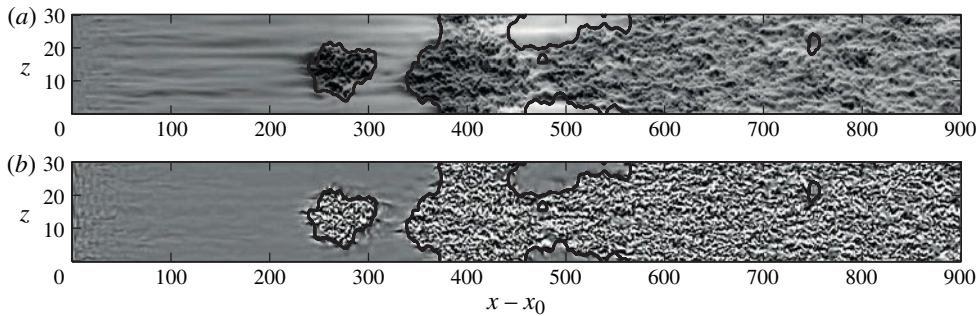


FIGURE 4. Laminar–turbulent edge detection plotted for a plan view of the boundary layer ( $y/\delta(x) \approx 0.5$ ) from a single snapshot from the ZPG case: (a)  $u'$  and (b)  $v'$ . The interface between the laminar and turbulent regions is marked by a solid dark grey line.

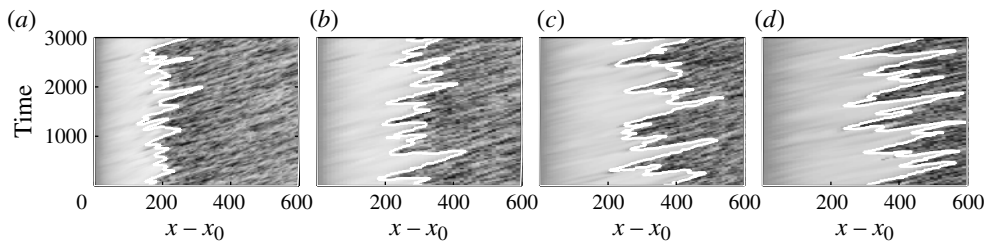


FIGURE 5. Time–space diagrams showing  $u'$  flow history for each case at  $y/\delta_0 = 0.7$  and  $z = 0$  for (a) strongly adverse to (d) favourable pressure gradient. The interface between the (light) laminar region and the (dark) turbulent region is marked in white.

the variance between laminar and turbulent events, but was unavailable to Hedley & Keffer at the time. The algorithm achieves this by calculating all possible thresholds and the resulting variances of each of the thresholded regions. The desired threshold is achieved by minimizing this *intra-class* variance, i.e. the variance within the laminar and turbulent zones. Otsu (1979) recognized that this could be achieved efficiently by maximizing the *inter-class* variance, i.e. the variance between the laminar and turbulent zones.

The output of the edge detection algorithm is shown in figures 4 and 5. Figure 4 is a visualization of the instantaneous flow field and the result of the laminar–turbulent discrimination. Here both the streamwise and wall-normal fluctuations are plotted. A solid line indicates the demarcation between the laminar ( $\Gamma = 0$ ) and the turbulent ( $\Gamma = 1$ ) regions. A distinct difference between the laminar and turbulent regions is observed, in particular for the wall-normal perturbations,  $v'$ . Here the laminar region appears smooth and shows little variation, while the turbulent region comprises high-frequency fluctuations. Figure 5 shows the identification of several turbulent spots in a time–space plot. This plot represents the time history of  $u'$  along a streamwise line at  $y = 0.7y/\delta_0$ . Here spots appear at some streamwise location and grow in time, tracing out a conical growth path. These regions eventually overlap and transition is complete. Upstream of the onset of turbulence, variation in the laminar region due to high-amplitude streaks is visible.

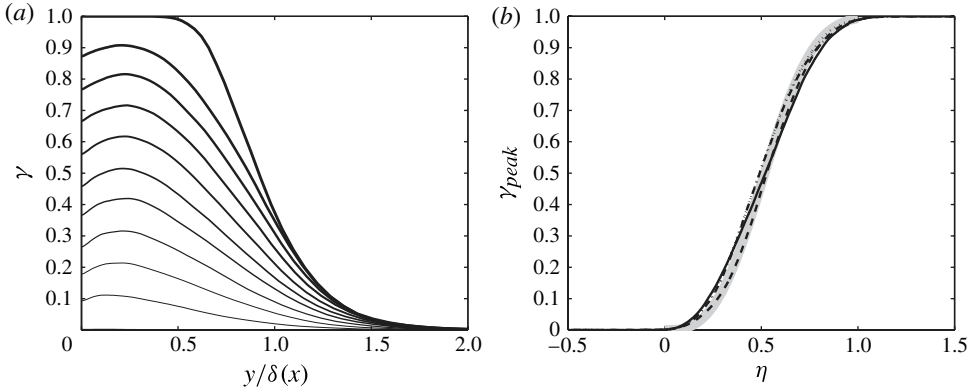


FIGURE 6. (a) Spanwise averaged wall-normal intermittency profiles at regular intervals,  $0.1\gamma_{peak}$ , throughout the transition region for the ZPG case. Line weight increases with increased downstream location. (b) Peak intermittency distributions for all cases normalized by the transition length,  $\eta = (x - x_s)/(x_e - x_s)$ , and compared to the expression  $\gamma_{peak} = 1 - \exp(-5\eta^3)$  by Abu-Ghannam & Shaw (1980) (grey curve). See figure 2 for legend.

The intermittency factor,  $\gamma$ , is the probability that the flow at a point is turbulent. Therefore,  $\gamma$  is initially zero for the pre-transitional region and increases to unity for the fully turbulent boundary layer. The intermittency can be evaluated from the mean of the logical indicator function,  $\Gamma$ , according to

$$\gamma(x, y, z) = \frac{1}{T} \int \Gamma dt. \quad (3.1)$$

In the current flow configuration, the intermittency is also averaged in the homogeneous spanwise direction and therefore  $\gamma = \gamma(x, y)$ .

### 3.2. Conditionally sampled flow statistics

The first statistic of interest is the intermittency factor,  $\gamma$ . Figure 6(a) shows wall-normal intermittency profiles for the zero pressure gradient case at a series of streamwise locations corresponding to 10% steps in the wall-normal maximum of the intermittency,  $\gamma_{peak}$ . The value of  $\gamma_{peak}$  increases steadily in the streamwise direction from zero in the pre-transitional region, to unity where transition to turbulence is complete. The wall-normal profiles increase from zero at the wall and plateau at  $y/\delta \approx 0.3$  before they decay to zero at  $y/\delta \approx 1.5$ . This remains the case even when the peak wall-normal intermittency is unity. The gradual decay in  $\gamma$  towards zero in the free stream is due to the irregular nature of the instantaneous turbulent boundary-layer edge.

The streamwise variation in the peak wall-normal intermittency is shown in figure 6(b), for all cases. As observed in the measurements of Abu-Ghannam & Shaw (1980), the intermittency distributions are remarkably self-similar and fall on  $\gamma_{peak} = 1 - \exp(-5\eta^3)$ , where  $\eta$  is the transition length,  $\eta = (x - x_s)/(x_e - x_s)$ . Subscripts  $s$  and  $e$  denote the start and end of transition, defined here as  $\gamma_{peak} = 0.005$  and  $\gamma_{peak} = 0.995$ , respectively. The shape of the intermittency distribution follows a sigmoid, which suggests an initial rapid growth followed by a much reduced growth rate. This reduction can be attributed to the continuously diminishing non-turbulent region for turbulent spots to occupy.

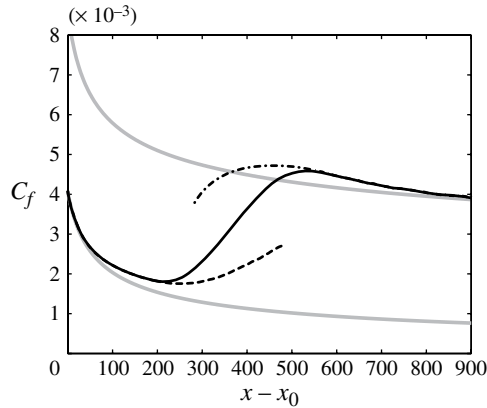


FIGURE 7. Conditionally sampled skin friction for *ZPG* case: laminar-conditioned data (dashed); turbulent-conditioned data (dash-dotted); laminar and turbulent predictions as in figure 2 (grey).

Emmons (1951) proposed that time-averaged quantities in intermittent flows can be considered as a combination of the contributions of the turbulent and non-turbulent components, weighted on the local intermittency factor:

$$f = (1 - \gamma)f_{LAM} + \gamma f_{TURB}. \quad (3.2)$$

Dhawan & Narasimha (1958) note that (3.2) is exact for the mean velocity and therefore for skin friction, while it is approximate for the integral thicknesses and shape factor.

The conditionally sampled skin friction for the zero pressure gradient case is plotted in figure 7. The laminar-conditioned data start at the Blasius level at the inlet, and slightly increase downstream due to the mean flow distortion by Klebanoff streaks. A more pronounced increase in the laminar-conditioned skin friction is observed after the onset of transition, and is explained below. The turbulent-conditioned data start at a lower value than the turbulent correlation. This should be distinguished from the results by Park *et al.* (2012), who computed their conditionally sampled turbulent skin friction by averaging over the entire spot footprint. The behaviour of the laminar- and turbulent-conditioned data in figure 7 is explained by considering the instantaneous skin friction. An example is presented in figure 8. The upper panels show streamwise and spanwise slices of a single turbulent spot observed in the *ZPG* case. The lower panels plot the corresponding instantaneous skin friction across the spot.

The pronounced rise in laminar  $C_f$  is seen in the plot of the instantaneous skin friction versus downstream distance, and is due to the ‘calmed’ flow trailing turbulent regions. Within the turbulent spot, the skin friction curve fluctuates about the turbulent correlation. However, at the spot periphery, i.e. the leading edge and the ‘wing tips’, the skin friction, although oscillatory, is at a lower level than the turbulent value. As a result, turbulent-conditioned skin friction near the onset of transition is on average lower than the turbulent correlation. Further downstream, as the spots spread and merge, the influence of their periphery diminishes and the skin friction increases.

The conditionally sampled integral displacement and momentum thicknesses,  $\delta^*$  and  $\theta$ , are shown in figure 9, and are compared to those of the Blasius solution. The decomposition into laminar and turbulent components reveals the relative contributions

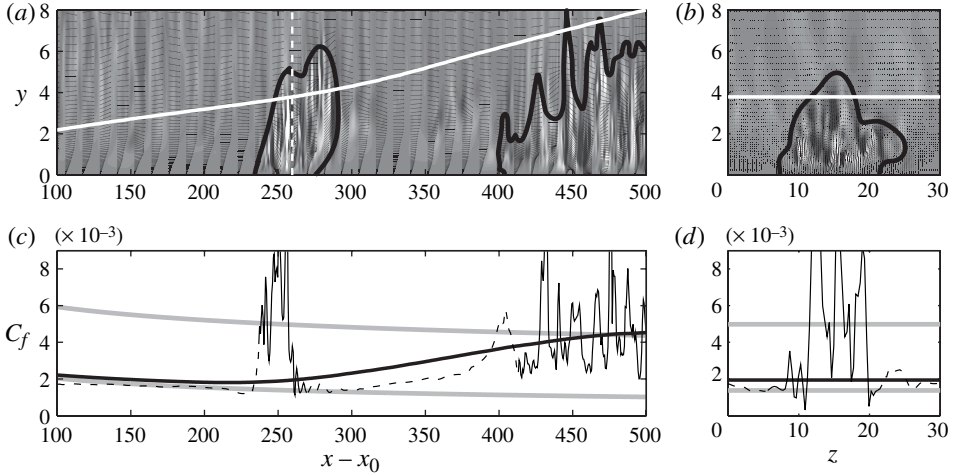


FIGURE 8. Instantaneous skin friction due to a single turbulent spot in the *ZPG* case. (a) Streamwise slice through the centreline of a spot, contoured by  $v'$ : mean boundary-layer edge,  $\delta_{99}$  (solid white); laminar-turbulent interface (solid black); location of spanwise slice (dashed white). (b) Spanwise slice through the spot. Corresponding (c) streamwise and (d) spanwise distributions of skin friction for laminar-conditioned data (dashed) and turbulent-conditioned data (solid black).

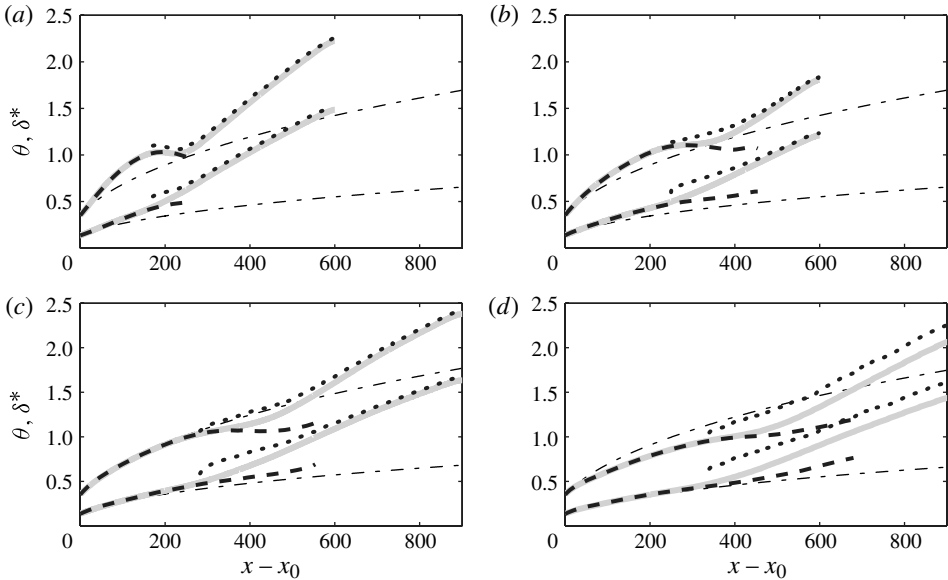


FIGURE 9. Conditionally sampled integral thicknesses,  $\delta^*$  and  $\theta$ , for (a) *APG\_strong*, (b) *APG*, (c) *ZPG* and (d) *FPG* cases: time-averaged (solid grey); laminar-conditioned (dashed); turbulent-conditioned (dotted); Blasius solution (dash-dotted).

to the change in the boundary-layer thickness during transition. The laminar-conditioned data, which correspond to the streaky flow surrounding turbulent spots, follows the theoretical solution upstream of transition. In the case of the displacement

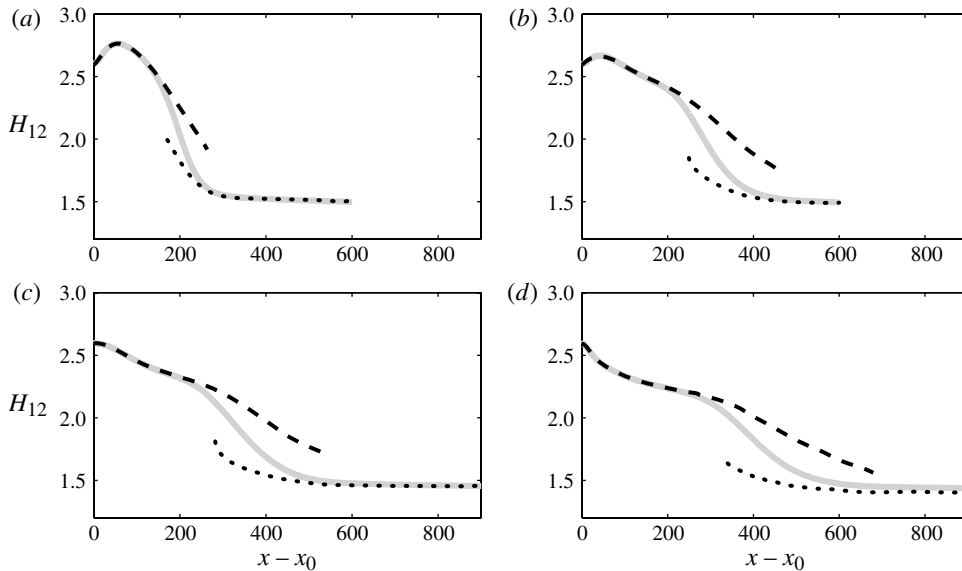


FIGURE 10. Conditionally sampled shape factor  $H_{12}$  for the integral thickness in figure 9 for (a)  $APG_{strong}$ , (b)  $APG$ , (c)  $ZPG$  and (d)  $FPG$  cases.

thickness, the laminar  $\delta^*$  reduces in the transition region. This behaviour is reflected in the decreasing shape factor  $H_{12}$  from the Blasius state ( $H_{12} = 2.59$ ) shown in figure 10. Matsubara & Alfredsson (2001) report similar decay of shape factor in their experiments. This decay is due to the distortion of the laminar boundary layer by streaks, and is further enhanced in the transition region by the inclusion of the high-speed calmed region trailing the turbulent spots in the laminar-conditioned data. For the adverse pressure gradients, there is an initial growth in shape factor similar to that reported by Abu-Ghannam & Shaw (1980). The turbulent-conditioned shape factor rapidly and consistently approaches  $H_{12} \approx 1.4$  for all cases.

### 3.2.1. Mean velocity profiles

The downstream evolution of the mean streamwise velocity  $U$  is shown in figure 11. Plotted in wall coordinates, the unconditioned time-averaged velocity profiles, shown in figure 11(a), gradually transition from a laminar to a fully turbulent profile as they steadily approach the law of the wall,  $U^+ = 1/\kappa \ln Y^+ + B$  where  $\kappa = 0.41$  and  $B = 5$ . For reference, a mean velocity profile from the turbulent boundary-layer DNS of Schlatter *et al.* (2009) at a Reynolds number  $Re_{\theta} = 670$  is shown. This corresponds to the end of the transition region in the present  $ZPG$  case ( $\gamma = 0.9$ ). The simulations of Schlatter *et al.* (2009) achieve a fully turbulent flow by tripping the boundary layer near the leading edge. Excellent agreement with wind tunnel experiments tripped similarly was reported in their work. In the context of the present simulations, the fully turbulent flow is achieved via bypass transition due to free stream buffeting of the boundary layer. Very good agreement is observed nonetheless.

The laminar- and turbulent-conditioned mean velocities exhibit distinct laminar and turbulent profiles, respectively. The laminar-conditioned velocity profiles (figure 11b) do not approach a turbulent state even up to the end of transition and retain a characteristic laminar shape, but are not self-similar due to the distortion by the streaks

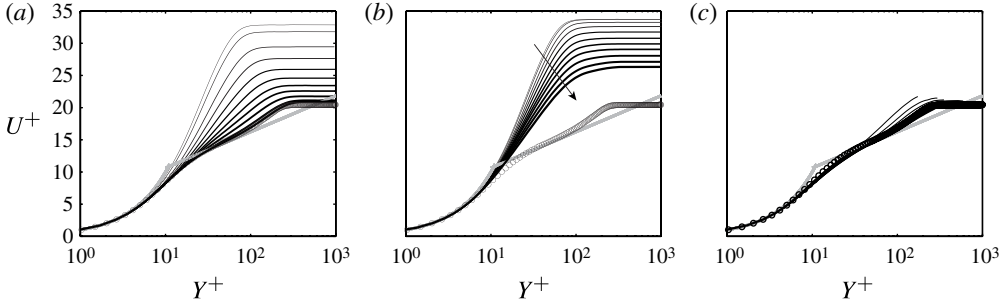


FIGURE 11. Mean velocity profiles for (a) time-averaged, (b) laminar-conditioned and (c) turbulent-conditioned data at the same streamwise locations as in figure 6. Line weight increases with increased intermittency. Symbols show the mean velocity profiles from the turbulent boundary-layer profiles of Schlatter *et al.* (2009) at the same Reynolds number ( $Re_\theta = 670$ ) corresponding to the end of transition.

and the calmed region that trails turbulent spots. On the other hand, the turbulent-conditioned velocity profiles (figure 11c) immediately and consistently follow the law of the wall throughout the transition region.

### 3.2.2. Reynolds stresses

The decomposition of the Reynolds stress into its constituent laminar and turbulent components is given by the following expression (Pope 2001):

$$\begin{aligned} \overline{u'_i u'_j} &= (1 - \gamma) \overline{u'_i u'_j}_{LAM} + \gamma \overline{u'_i u'_j}_{TURB} \\ &+ \gamma(1 - \gamma)(\overline{u}_{iTURB} - \overline{u}_{iLAM})(\overline{u}_{jTURB} - \overline{u}_{jLAM}). \end{aligned} \quad (3.3)$$

Equation (3.3) can be understood by considering the time series in figure 12, which shows a record of the total velocity,  $u(t)$ , close to the wall, for the ZPG case in the transition region. This plot is similar to the recording by a hot-wire sensor in an experiment. The indicator function,  $\Gamma$ , is also shown and identifies regions of turbulent flow ( $\Gamma = 1$ ), which are characterized by high-frequency fluctuations. Turbulent regions have a high variance about the turbulent mean (indicated by the upper dashed line and shaded region), unlike the quiescent laminar regions. However, the unconditioned time-averaged data contain both laminar and turbulent regions, both offset from the time-averaged mean (indicated by a dash-dotted line). The variance of the unconditioned signal (indicated by a brace) as a whole may be greater than the turbulent-conditioned data alone. In order to reconstruct the total signal variance from the laminar and turbulent signals, the offset of these variances from the time average must be taken into account using (3.3).

Conditioned and unconditioned velocity profiles are shown in figure 13 for the ZPG case at  $\gamma_{peak} = 0.5$ , corresponding to the midpoint in the transition region. Here the flow has an equal probability of being in a turbulent or non-turbulent state. The conditional mean velocity profiles are computed using (3.2) while the conditional Reynolds stresses are evaluated using (3.3). The unconditional and intermittency weighted profiles show excellent agreement. The turbulent-conditioned  $\overline{u'u'}$  profile exhibits a consistent turbulent shape, with an acute near-wall peak, similar to the time-averaged data at the end of transition. However, it is noteworthy that the magnitude

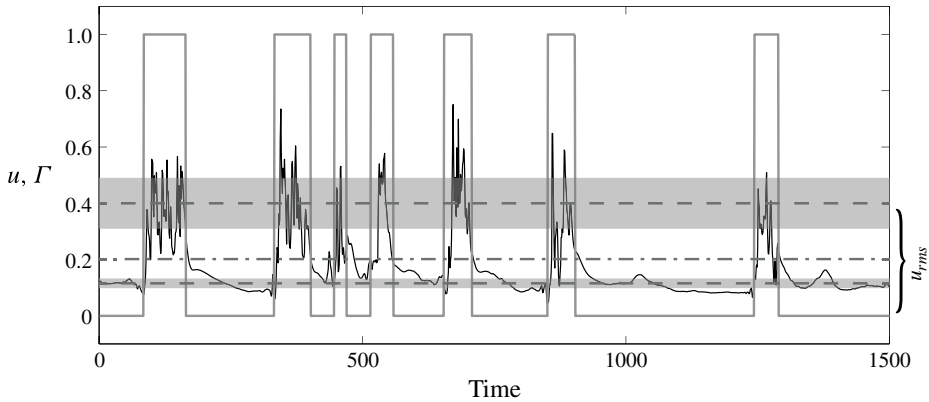


FIGURE 12. Time series from ZPG case showing intermittent total velocity history,  $u(t)$ . The indicator function,  $\Gamma$ , identifies periods of laminar ( $\Gamma = 0$ ) and turbulent flow ( $\Gamma = 1$ ). The laminar and turbulent means are indicated by dashed lines, while the dash-dotted line indicates the time-averaged mean. Shaded regions indicate the extent of the second moment about the laminar and turbulent means, while the brace indicates the r.m.s. of the signal as a whole.

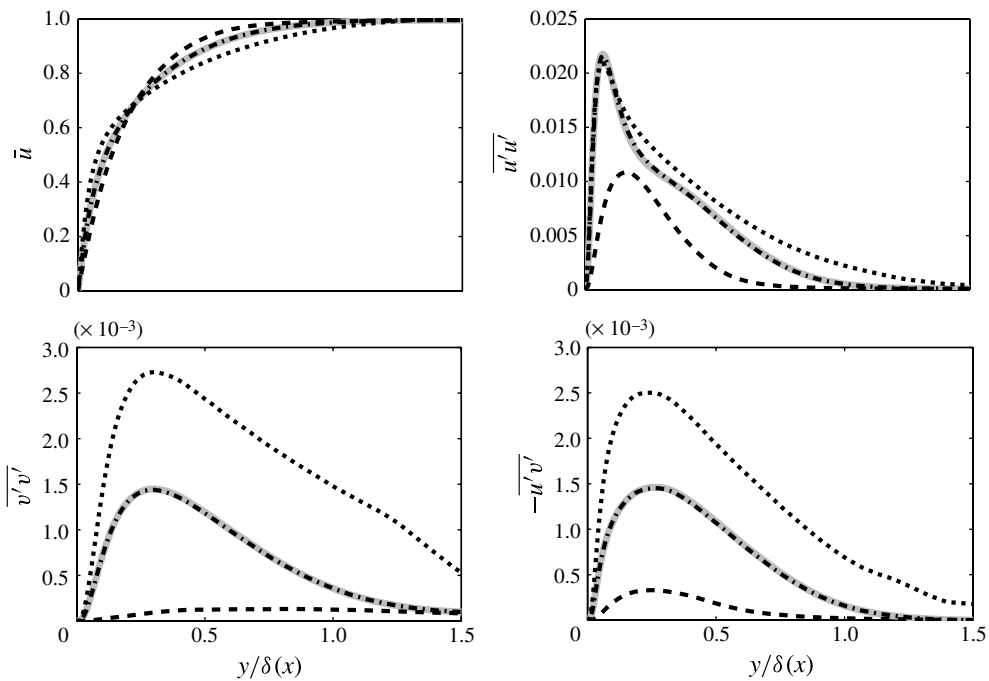


FIGURE 13. Weighted velocity profiles for ZPG case at  $\gamma_{peak} = 0.5$ : time-averaged (solid grey); laminar-conditioned (dashed); turbulent-conditioned (dotted); intermittency-weighted (dash-dotted).

of the peak is decaying as transition progresses. The laminar-conditioned  $\overline{u'u'}$  profile differs in magnitude from the other Reynolds stresses due to the streamwise dominance of the streaks.

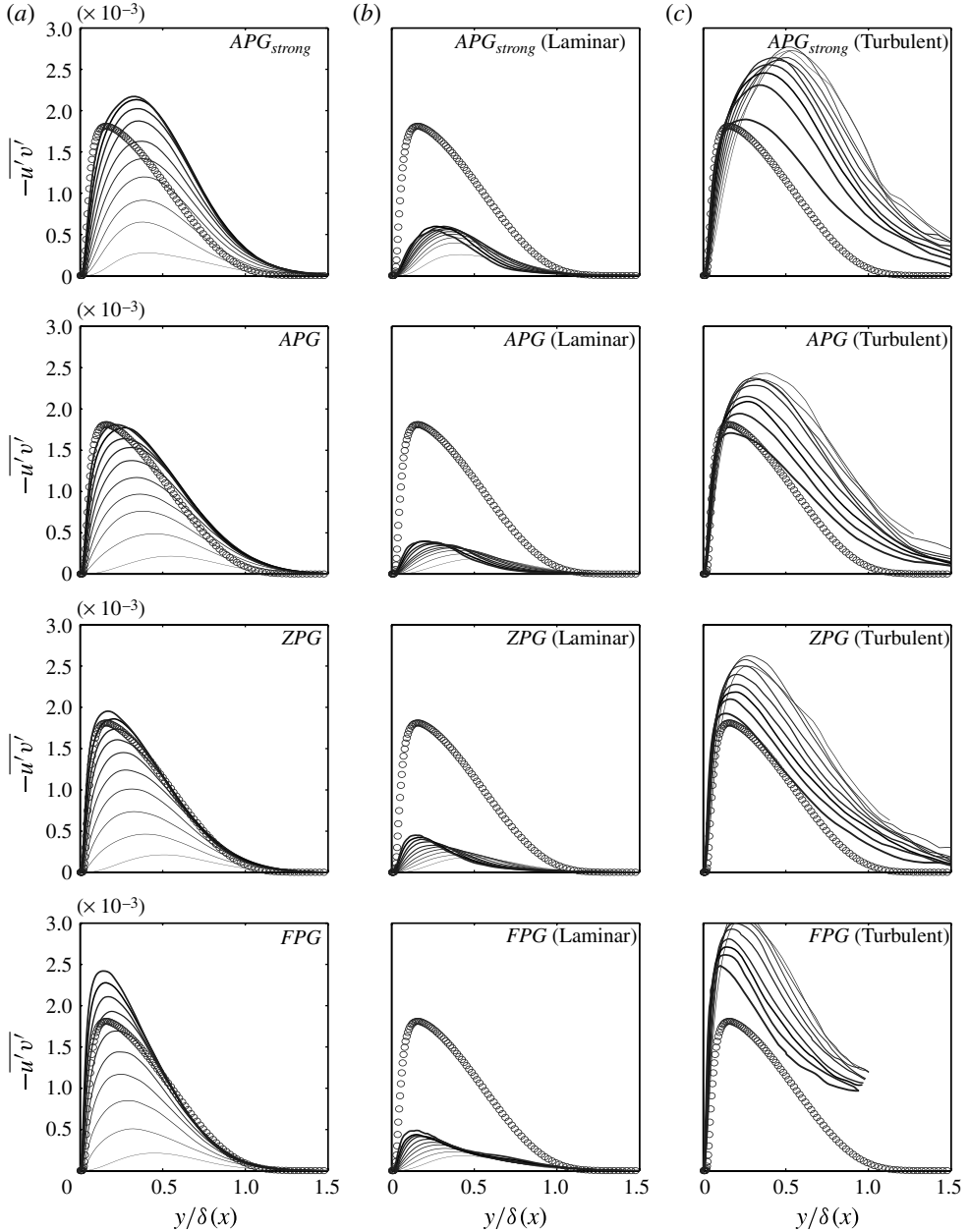


FIGURE 14. Conditionally sampled Reynolds shear stresses for each pressure gradient plotted at regular peak intermittencies after figure 6. As above, increased line weight indicates higher intermittency factor. Symbols show the corresponding Reynolds stress for the fully turbulent boundary-layer simulations of Schlatter *et al.* (2009).

Conditionally sampled Reynolds shear stresses are plotted in figure 14 for a range of intermittencies,  $0.1 < \gamma_{peak} < 0.9$ . Both conditional and unconditional profiles are shown for each pressure gradient. The time-averaged data show a smooth but significant growth in magnitude across the transition region with good agreement with

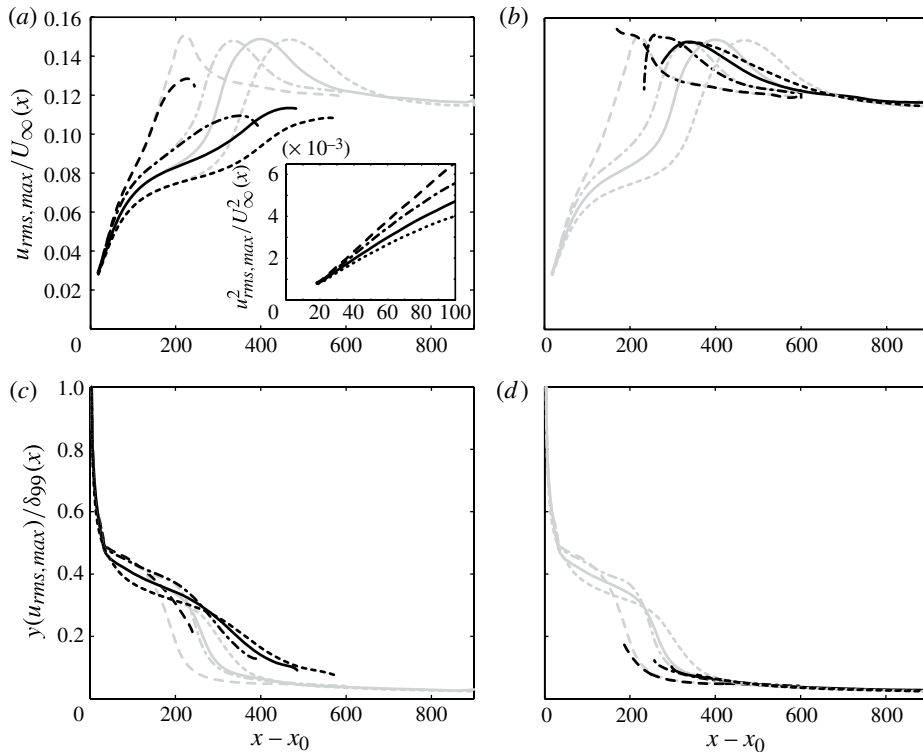


FIGURE 15. (a,b) Downstream evolution of the conditionally sampled peak  $u_{rms}/U_{\infty}(x)$  for all cases: (a) laminar- and (b) turbulent-conditioned data. The inset shows that  $u_{rms}^2$  scales linearly with downstream distance. (c,d) The corresponding wall-normal location of the maximum. Line types have the same meaning as in figure 3.

the simulations of Schlatter *et al.* (2009) for the ZPG case. The laminar-conditioned data show limited growth compared to the  $\overline{u'u'}$  profiles observed in figure 14, due to the streamwise dominance of the streaks. The turbulent-conditioned data are consistently higher than the reference data of Schlatter *et al.* (2009). There is some early growth in magnitude followed by a steady decay towards the turbulent boundary-layer reference data. The apparent growth observed in the time-averaged data can therefore be attributed to the weighting effect of the local intermittency as expressed in (3.3).

### 3.2.3. Disturbance growth

The wall-normal peak of  $u_{rms}$  is reproduced in figure 15 with the conditionally sampled data superimposed. This allows the growth in streak intensity, as estimated by the laminar-conditioned  $u_{rms}$ , to be evaluated without contamination from surrounding turbulent spots.

Considering the laminar-conditioned results, the inset in figure 15 shows the linear energy growth in the early evolution of the streaks, consistent with previous studies of bypass transition (e.g. Matsubara & Alfredsson 2001). In addition, the laminar-conditioned  $u_{rms}$  curves do not exhibit the pronounced secondary growth that is observed in the unconditionally sampled data. Instead, the laminar curves reach a peak near the end of the laminar region. Should transition to turbulence not take place,

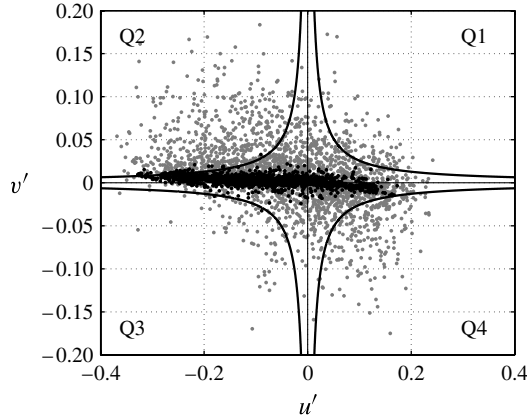


FIGURE 16. Scatter plot of conditionally sampled data at  $y/\delta(x) = 0.5$ . The laminar conditioned data (black) are confined to the streamwise perturbation, while the turbulent conditioned data (grey) are scattered across both components and primarily in quadrants 2 and 4. Shown also are contours of constant shear stress  $H(u'_{rms}v'_{rms})$ ,  $H = 1$ . Data lying outside these curves satisfy the hole region for the constant  $H$ .

it is expected that the streaks would decay due to viscous effects, in a manner similar to that described by Zaki & Durbin (2006).

The turbulent-conditioned data follow a trend similar to that of the secondary peak and therefore the shape may be attributed to the growth and subsequent maturation of turbulent spots rather than streak amplitude. As in figure 14, the magnitude shows an initial growth and is followed by a decay towards a fully turbulent level. Moreover, while the turbulent-conditioned data follow the shape of the unconditional secondary peak, they are somewhat lower in magnitude. This is related to the inclusion of mean velocity terms in (3.3) as discussed above.

### 3.3. Quadrant analysis

Quadrant analysis allows the contributions to the Reynolds shear stress from different events to be quantified. By splitting the conditionally sampled perturbation data into quadrants, the effects of lift-up and the structure of turbulent spots on the boundary layer may be investigated (figure 16). In turbulent channel flow, Wallace, Eckelmann & Brodkey (1972) identified ‘ejections’ (Q2,  $-u', +v'$ ) and ‘sweeps’ (Q4,  $+u', -v'$ ) as the primary characteristic of events that contribute to the wall-normal transport of momentum. Sweeps were reported by Willmarth & Lu (1972) as predominant close to the wall and ejections strongest at the edge of the turbulent boundary layer. Quadrant analysis of conditionally sampled data can help to understand the type of structures that make up turbulent spots.

A scatter plot of the distribution of fluctuations at a point in the transitional boundary layer is presented in figure 16 ( $\gamma = 0.5$ ,  $y/\delta_{99} = 0.5$ ). The laminar-conditioned stresses, shown by black points, remain confined to streamwise perturbations. The turbulent-conditioned data, shown by grey points, display significant wall-normal perturbations, predominantly due to Q2 and Q4 events.

The contribution of each quadrant to the Reynolds shear stress,  $\overline{u'v'}$ , is shown in figure 17. The data correspond to the streamwise location  $\gamma_{peak} = 0.5$ , and are

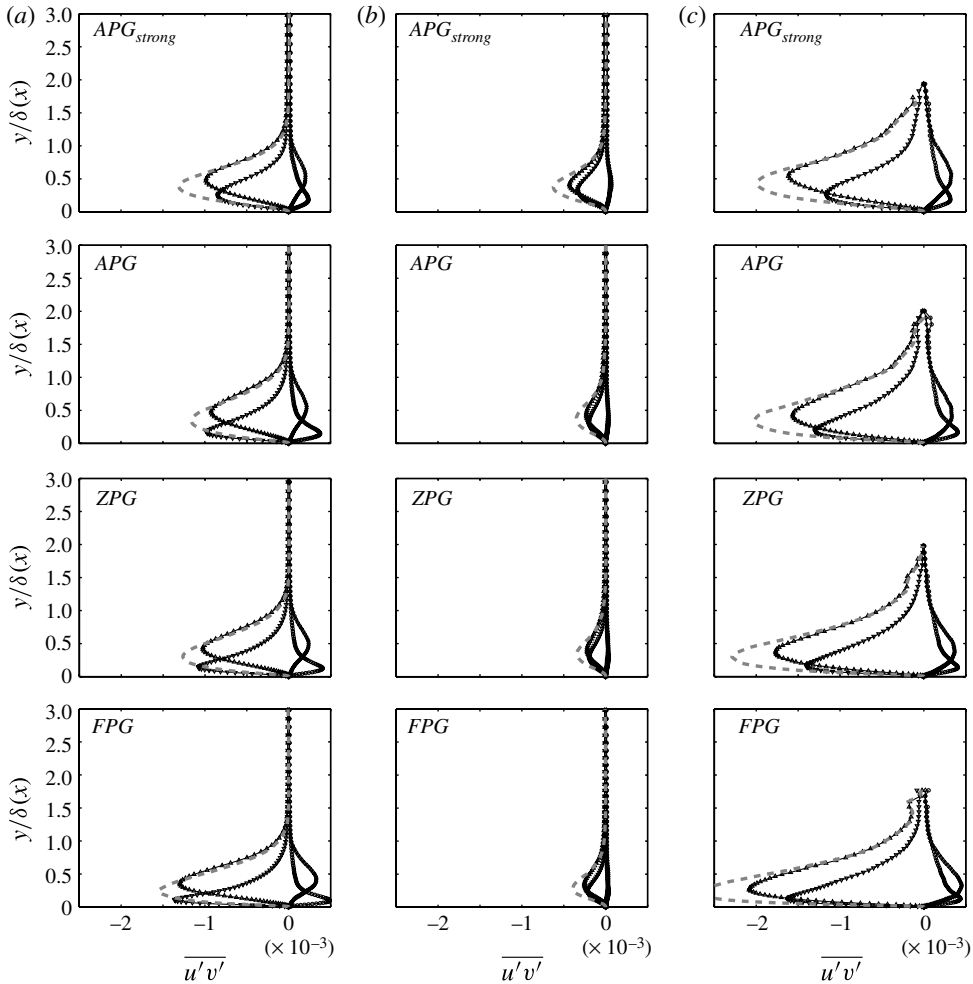


FIGURE 17. Quadrant decomposed  $\overline{u'v'}$  profiles at  $\gamma = 0.5$  for each case for (a) time-averaged data, (b) laminar-conditioned data, and (c) turbulent-conditioned data:  $\circ$ , Q1;  $\triangle$ , Q2;  $\diamond$ , Q3;  $\nabla$ , Q4; total  $\overline{u'v'}$  shown by dashed line.

decomposed into laminar- and turbulent-conditioned data. For the unconditioned data, it is observed that Q4 sweeps and Q2 ejections are predominant and contribute most to the total Reynolds shear stress. Both sweeps and ejections grow significantly and at similar rates as transition progresses. As previously noted, sweeps peak close to the wall while ejections peak away from the wall. The wall-normal maxima move away from the wall with increasingly adverse pressure gradient.

Based on figure 17 the laminar-conditioned Reynolds shear stress is relatively small, although sweeps and ejections remain most dominant. The strongest adverse case exhibits higher amplitudes than the other pressure gradients. The turbulent-conditioned data in figure 17 are more interesting. Here, ejections show higher peak values than sweeps. The same observation can be made at all stages through the transition region, due to the fuller turbulent-conditioned mean velocity profile (not shown).

### 3.4. Quadrant hole analysis

Quadrant hole analysis demonstrates how intermittent, but high-amplitude, events can contribute significantly to the total Reynolds shear stress. A threshold is selected based on multiples of constant shear stress,  $H(u_{rms}v_{rms})$ , and the contribution of data exceeding this threshold to the shear stress is computed. Willmarth & Lu (1972) and Nolan *et al.* (2010) describe the method in detail. Figure 16 shows lines of constant shear stress. Data falling outside these curves exceed the prescribed threshold and are described by an indicator function,  $I_H^i$ . The percentage time spent beyond the threshold in quadrant  $i$  is called the duration fraction and is given by

$$D_H^i = \frac{1}{N} \sum_{n=1}^N I_{H,n}^i, \quad i = 1, \dots, 4, \quad (3.4)$$

so that

$$\sum_{i=1}^4 D_H^i(H) + D_H^h(H) = 1. \quad (3.5)$$

Here  $N$  is the number of samples and the superscript  $h$  refers to the data within the hole region. The percentage contribution to the shear stress from the data exceeding the threshold in quadrant  $i$  is defined as the stress fraction,

$$\frac{\widetilde{u'v'_i}(H)}{\overline{u'v'}} = \frac{1}{\overline{u'v'}} \frac{1}{N} \sum_{n=1}^N u'v'_i(t) I_H^i, \quad i = 1, \dots, 4, \quad (3.6)$$

so that

$$\sum_{i=1}^4 \frac{\widetilde{u'v'_i}(H)}{\overline{u'v'}} + \frac{\widetilde{u'v'_h}(H)}{\overline{u'v'}} = 1. \quad (3.7)$$

Typically, rare events found at high thresholds can have significant contributions to the Reynolds shear stress in fully turbulent boundary layers, as noted by Willmarth & Lu (1972) (although their results potentially overestimated this contribution due to their measurement probe). One advantage of the quadrant hole method is that the laminar contribution is quickly filtered out as the threshold grows: as can be seen in figure 16, the laminar data lie within the ‘hole’ region.

Figure 18 shows shaded contours of the stress fraction and contour lines of the duration fraction for each pressure gradient condition. Based on the current results, approximately 20% of the Reynolds shear stress  $\overline{u'v'}$  results from less than 5% of the time. In addition, for large hole size, we observe that high-amplitude Q2 events, although rare, still contribute appreciably to the Reynolds shear stress. There is a strong similarity across all the pressure gradient cases throughout the transition region. Ejections show the largest peak at the boundary-layer edge throughout. Close to the wall, sweeps also show a strong peak. This behaviour was also reported in the particle image velocimetry (PIV) measurements of Nolan *et al.* (2010).

## 4. Laminar streaks

The traditional statistical method for estimating streak amplitude is calculating  $u_{rms}$ , as presented in figure 15. However, the r.m.s. does not differentiate between positive and negative streaks, which led several researchers to propose using the maximum

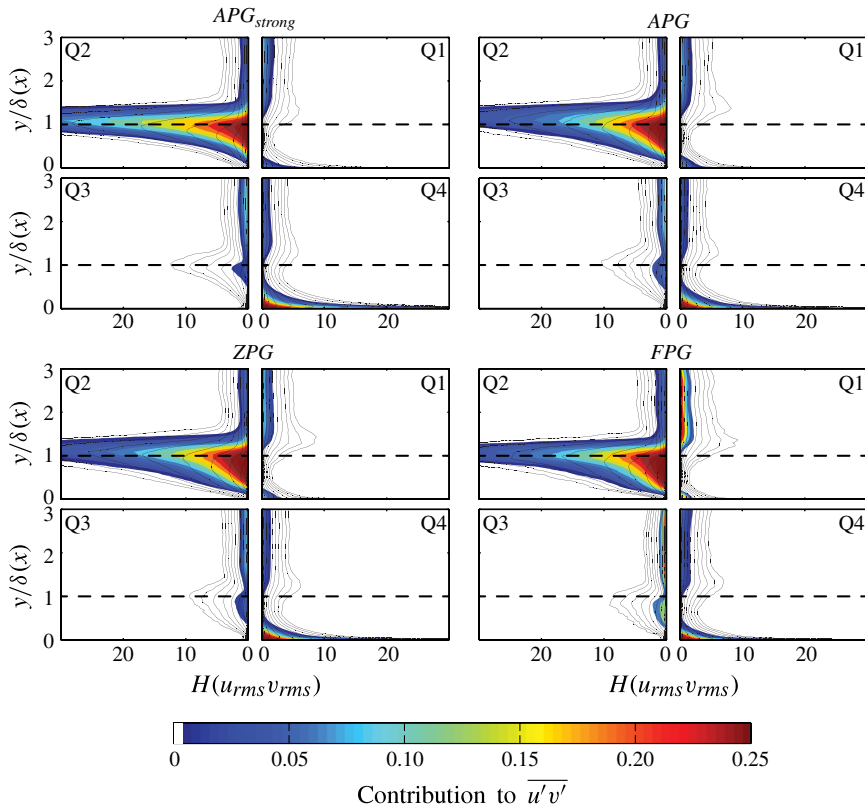


FIGURE 18. Quadrant hole  $\widetilde{u'v'}$  profiles. Colour contours of stress fraction and solid contour lines of duration fraction for each case at  $\gamma = 0.5$ . The duration fraction contour lines step from 25 to 0.1% logarithmically [25%, 13.5%, 7.3%, 3.9%, 2.1%, 1.2%, 0.63%, 0.34%, 0.18%, 0.1%].

and minimum of the distribution of the perturbation history as an indicator of streak amplitude (Wundrow & Goldstien 2001; Hernon *et al.* 2007; Nolan & Walsh 2012). This approach, however, is wasteful of data and carries the risk of the data being biased by a small number of observations, e.g. the peak of a particularly strong streak.

Another important consideration is that streaks are low-frequency events, of large streamwise extent. As a result, single streaks may be sampled repeatedly in both time and space when computing the r.m.s. These data are therefore highly correlated. Consequently, the assumption of independent, identically distributed (i.i.d.) observations, which may hold somewhat for sampling of high-frequency turbulent flows, is not necessarily valid when estimating streak amplitudes from the distribution of  $u'$ . In order to determine the influence of streaks on the breakdown to turbulence, individual events must be considered. This requires the identification of individual streaks in both space and time. The ability to identify and track a particular streak event is also required in order to directly measure the critical streak amplitude for breakdown to turbulence.

#### 4.1. Streak detection

Lin *et al.* (2008) identified individual streaks in stereo PIV measurements of the viscous sublayer of a turbulent boundary layer. Regions of high- and low-speed

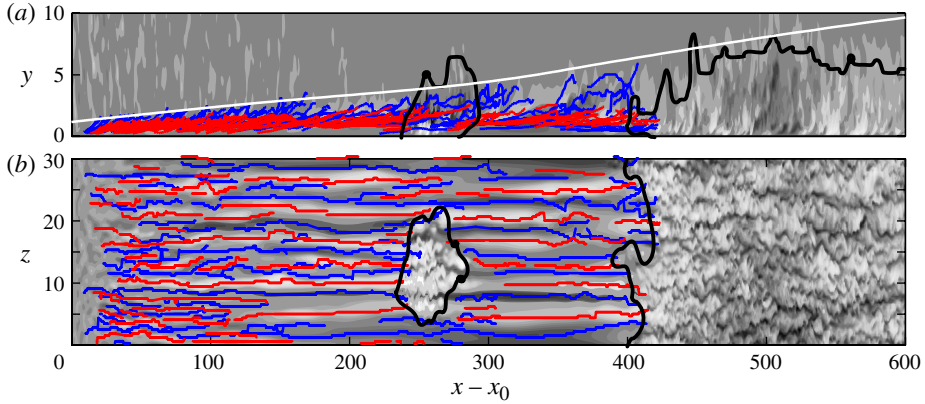


FIGURE 19. (a) Side and (b) plan views with the identification of positive (red) and negative (blue) streaks. The side view is in the plane of symmetry of the turbulent spot, and the plan view is located at  $y/\delta_0 = 0.7$ . Shown also is the laminar–turbulent edge detection (black) and the mean boundary-layer thickness (white).

fluid were isolated and properties such as spanwise angle, spacing and width were catalogued. Marquillie, Ehrenstein & Laval (2011) utilized a skeletonization technique to identify the centreline of individual streaks in their numerical simulations. Here we present a robust algorithm to isolate individual streaks in the DNS velocity fields and to extract the velocity perturbation along their streamwise extent, thus providing a true measure of streak amplitude.

Boundary-layer streaks are dominated by the streamwise perturbation velocity, as noted by Jacobs & Durbin (2001). Therefore, the first step in the streak detection algorithm is identification of local extrema in the  $u'$  perturbation field at every streamwise plane. Local extrema that are attributed to the free stream turbulence, and not to boundary-layer streaks, must be removed. This requires evaluation of the instantaneous boundary-layer edge. Here the criterion  $u_\delta = 0.95U_\infty(x)$  is selected and a spatial filter is applied to eliminate any isolated regions to retain a single contiguous interface between the boundary layer and the free stream. All the local extrema beyond the instantaneous boundary-layer edge are discarded. Neighbouring extrema that are connected in successive streamwise planes are connected and are labelled as a unique object. Figure 19 shows the typical output of the streak detection algorithm. Both a wall-normal and a spanwise slice through an instantaneous  $ZPG$  field are shown. The contours represent the  $u'$  perturbation field. The laminar–turbulent discrimination demarcates the interface between the streaky laminar boundary layer and the turbulent flow. Red and blue lines indicate the spatial coordinates of the detected positive and negative streaks, respectively. Negative streaks are observed to be lifted towards the boundary-layer edge, while positive streaks remain close to the wall.

Streaks are tracked in time by cross-correlating the amplitude signature of each streak in a snapshot with those in the following snapshot. Thus a temporal connection table is created, which links instances of each unique streak throughout its evolution. In this manner, streaks can be regarded as Lagrangian objects. For each streak,  $s$ , its spatial coordinates are known as a function of time,  $\mathbf{x}^s(t)$ , and the streak amplitude during its evolution is defined by

$$\mathcal{A}_u^s(\mathbf{x}^s, t) \equiv u'(\mathbf{x} = \mathbf{x}^s, t). \quad (4.1)$$

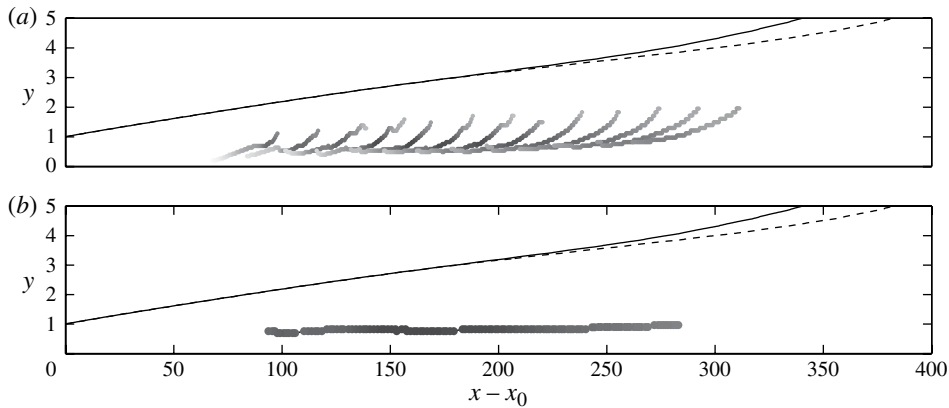


FIGURE 20. (a) Side view showing a single positive streak's temporal evolution. Streak instances corresponding to every 20 convective time units are shown. The data are 'coloured' by streak amplitude,  $\mathcal{A}_u^s$ , from light to dark. (b) Plot of  $A_u^s$  obtained with (4.2) versus  $y^s$ . Shown also are the mean boundary edge (solid line) and the laminar conditioned boundary-layer edge (dashed line).

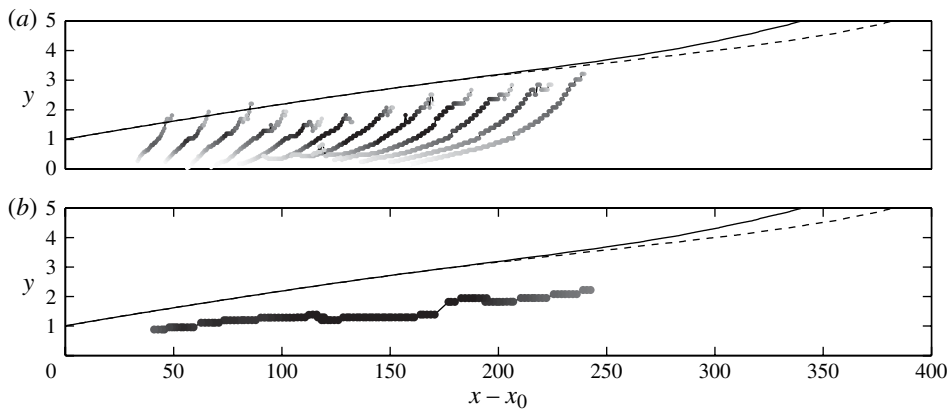


FIGURE 21. Temporal evolution of a negative streak as in figure 20.

Examples of the time history of a positive and a negative streak are presented in figures 20 and 21, respectively. Panel (a) in each shows a side view of the streak coordinates, 'coloured' by the amplitude,  $\mathcal{A}_u^s(\mathbf{x}^s, t)$ . At every streamwise position, we extract the maximum amplitude of the streak throughout its time history,

$$A_u^s(x) = \begin{cases} \max_{t,y,z}(\mathcal{A}_u^s(\mathbf{x}^s, t)) & \text{for } \mathcal{A}_u^s > 0, \\ \min_{t,y,z}(\mathcal{A}_u^s(\mathbf{x}^s, t)) & \text{for } \mathcal{A}_u^s < 0, \end{cases} \quad (4.2)$$

and the wall-normal position of this maximum,

$$y^s(x) = y(A_u^s(x)). \quad (4.3)$$

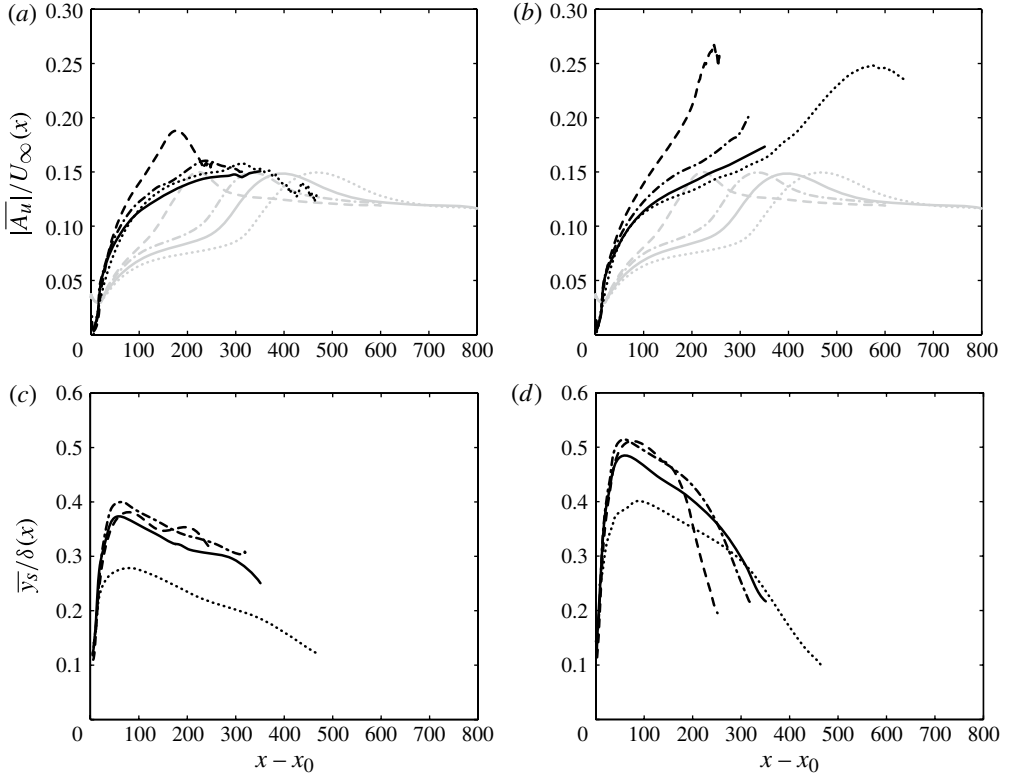


FIGURE 22. (a,b) Averaged streak amplitude of isolated (a) positive and (b) negative streaks. The  $u_{rms}$  profiles in figure 3 are also reproduced in grey. (c,d) Streamwise variation of  $y^s$  for each case. See figure 2 for legend.

Examples of  $y^s(x)$  are shown in figures 20 and 21, respectively. The location of  $y^s(x)$  for the high-speed streak is near the wall, and closer to the boundary-layer edge for the low-speed example.

#### 4.2. Streak amplitude

The mean streak amplitude,  $\overline{A}_u$ , is shown in figure 22,

$$\overline{A}_u = \frac{1}{S} \sum_{s=1}^S A_u^s. \quad (4.4)$$

It is evident that  $\overline{A}_u$  is significantly higher than  $u_{rms}$ , which is reproduced from figure 3. In addition, adverse pressure gradient enhances the streak amplitude:  $\overline{A}_u$  is approximately 30% higher for the adverse pressure gradient cases compared to the favourable case. Figure 22(c,d) show  $\overline{y}_s^s$  relative to the local boundary-layer thickness. Unlike the wall-normal location of maximum  $u_{rms}$  (figures 3 and 15), which represents where the most variance between streaks occurs, this represents the true position of the streaks within the boundary layer. The figure demonstrates that adverse pressure gradient displaces  $\overline{y}_s^s$  away from the wall – a result consistent with the observations by Marquillie *et al.* (2011) in the context of turbulent channel flow with a curved lower wall.

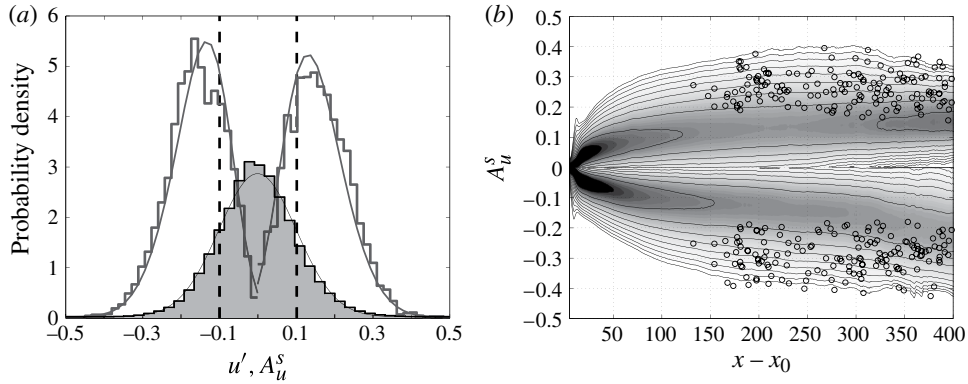


FIGURE 23. (a) Typical probability distribution of  $u'$  (grey shading) at wall-normal location of peak  $u_{rms}$  with fitted Gaussian distribution, and probability distributions of streak amplitude with fitted type I GEV. The r.m.s. level is indicated by the dashed lines. (b) Streamwise variation of the GEV distribution for the ZPG case. Contour lines are logarithmically spaced between decades  $10^{-0.25}$  to 10 in steps of  $10^{0.14}$ . Data points indicate the positive and negative streak amplitudes  $A_u$  in closest proximity to the turbulent spot inception location.

A fuller representation of the streak population is presented in figure 23, where the distribution of  $A_u^s$  is plotted at a fixed downstream location. The figure contrasts the current results to conventional measurements of the perturbation field. The distribution of  $u'$  fluctuations and  $u_{rms}$  are all shown. The distribution of streak amplitudes can be modelled using extreme value theory (Coles 2001). In an analogue to the central limit theorem, the distribution of the maximum (or minimum) of i.i.d. random variables is described by one of three possible distributions, which are often unified under the generalized extreme value (GEV),

$$G(z; \mu, \sigma, \xi) = \exp \left\{ - \left[ 1 + \xi \left( \frac{z - \mu}{\sigma} \right) \right]^{-1/\xi} \right\}, \quad (4.5)$$

where  $\xi$  is the shape parameter,  $\mu$  is the position parameter and  $\sigma$  is the width parameter.

Of these, the Gumbel distribution,  $\xi \rightarrow 0$ , is the limiting case of the exponential parent distributions, such as the normal distribution. In the case of streak amplitude (e.g. figure 23), the shape parameter tends to zero ( $\xi \rightarrow 0$ ), which results in a type I, or Gumbel, distribution for  $A_u^s$ . The parent distribution for this outcome is a Gaussian, which is consistent with the probability density function of  $u'$ .

The GEV models the maxima of the parent distribution and therefore only depends on the shape of its tail. This reinforces that the use of  $u_{rms}$  as an indicator of streak amplitude is inadequate because all positions in the streaks are sampled and the standard deviation, while somewhat sensitive to long tails, may be biased. As such,  $u_{rms}$  masks the probability of high-amplitude streaks (see figure 23).

Figure 23 also shows the streamwise development of the fitted GEV distributions  $A_u^s$ . The streak amplitude initially grows quickly for both positive and negative streaks, and the latter continue to grow steadily downstream. The width of the distributions increases, with streak amplitudes reaching as high as 40% of the local free stream velocity.

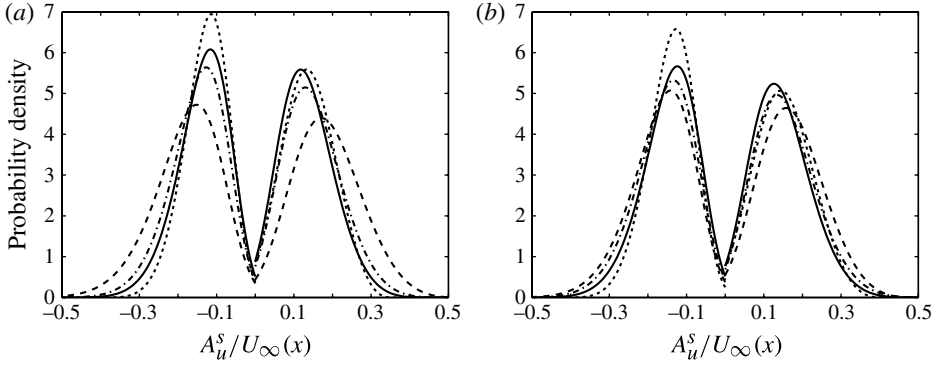


FIGURE 24. Distributions of each case at (a)  $x - x_0 = 150$  and (b) transition onset. Line styles as in figure 1.

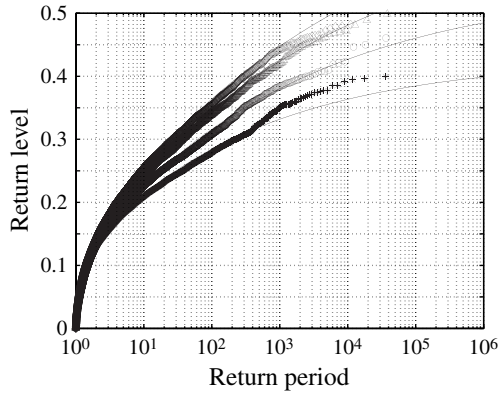


FIGURE 25. Return plots of negative streak amplitude at transition onset for all cases:  $APG_{strong}$  ( $\diamond$ );  $APG$  ( $\triangle$ );  $ZPG$  ( $\circ$ );  $FPG$  ( $*$ ). Streak amplitude is normalized by the local streamwise velocity,  $U_\infty(x)$ .

The effect of pressure gradient at a fixed position upstream of transition ( $x - x_0 = 150$ ) is shown in figure 24. The distribution of streak amplitudes shifts towards higher magnitudes with increasingly adverse pressure gradient. A similar trend is observed at the point of transition onset for each respective case.

It is informative to transform the results in the form of a return level plot (figure 25). This plot recasts the GEV of streak amplitudes in the form of a return level and an associated return period. The return level,  $z_p$ , is the streak amplitude and the return period,  $1/p$ , is the elapsed time between consecutive events of this amplitude. The expression for  $z_p$  is obtained by inverting (4.5):

$$z_p = \begin{cases} \mu - \frac{\sigma}{\xi} [1 - \{-\log(1 - p)\}^{-\xi}] & \text{for } \xi \neq 0, \\ \mu - \sigma - \log[-\log(1 - p)] & \text{for } \xi = 0, \end{cases} \quad (4.6)$$

where

$$p = 1 - G(z_p). \quad (4.7)$$

In the transitional boundary layer, the return level of interest is the streak amplitude immediately upstream of breakdown to turbulence. Using the conditional sampling techniques presented herein, both the coordinates of every incipient turbulent spot and the amplitude of its host streak are identified. Superimposed on figure 23(b) are data points representing the instantaneous amplitudes of both the low- and high-amplitude streaks in closest proximity to turbulent spot inception. It is found that turbulence onset is associated with  $A_u^s > 0.2$ , with the majority of breakdown events in the vicinity of  $A_u^s \sim 0.3$ .

Assuming  $z_p = 0.3$ , figure 25 illustrates that the associated return period decreases with adverse pressure gradient. Therefore, if breakdown to turbulence is a result of high-amplitude streaks, there should be a greater number of turbulent spots observed with increasingly adverse pressure gradient.

## 5. Turbulent spots

The results of conditional sampling as shown in figure 5 are reproduced in figure 26 in the form of a time–space diagram. The figure is strikingly similar to the high-density hot-film measurements of Anthony *et al.* (2005). Similar to that work, ‘faint tracks’ are observed in the laminar region and are due to the streaks.

The current simulations illustrate that, while many spot breakdowns may appear concentrated in a narrow streamwise window, there is a range of streamwise positions within the transition length where spots are initiated. This is reaffirmed in figure 26(b,c), which show histograms of spot inception locations and the intermittency profiles. These distributions are calculated by removing the turbulent boundary layer from the four-dimensional time–space data, of which figure 26 represents a slice, and determining the apex of the cone traced out by the spots. This cone extends from the point of spot inception to the point just prior to merging with the fully turbulent boundary layer or with other spots.

The wall-normal location of spot inception is reported in figure 26(c). Apart from the strong *APG* case, spot inception typically occurs in the outer half of the boundary layer, which is consistent with the ‘top-down’ breakdown scenario (Jacobs & Durbin 2001; Zaki & Durbin 2005). Typically, the majority of spots form in the first half of the transition region, as shown in figure 26(b). This is intuitive, as the remaining non-turbulent space for spots to form diminishes downstream. In addition, the figure clearly demonstrates a significant increase in the turbulent spot production rate with adverse pressure gradient. As a result, the boundary layer is rapidly saturated with turbulent spots and, therefore, the transition length is relatively short.

In the strong *APG* case, spots are initiated most frequently near the wall. The presence of an outer and an inner instability of streaky boundary layers was explained by Vaughan & Zaki (2011). The current results demonstrate the shift from outer to inner breakdown due to a strong adverse pressure gradient. This trend was also remarked upon by Marquillie *et al.* (2011) based on their stability analysis of streaks that were extracted from DNS of a turbulent channel with a curved lower wall.

In order to relate the initiation of localized breakdown to the streak amplitude, the results from figures 25 and 26 are combined in figure 27. The figure also serves as a summary of the current findings for all the pressure gradients considered. Firstly, the intermittency distribution and the histogram of spot inception count (figure 26b) are reproduced. In addition, the return periods for selected streak amplitudes ( $z_p \pm [0.1, 0.2, 0.3, 0.4]$ ) are plotted versus downstream distance. For a

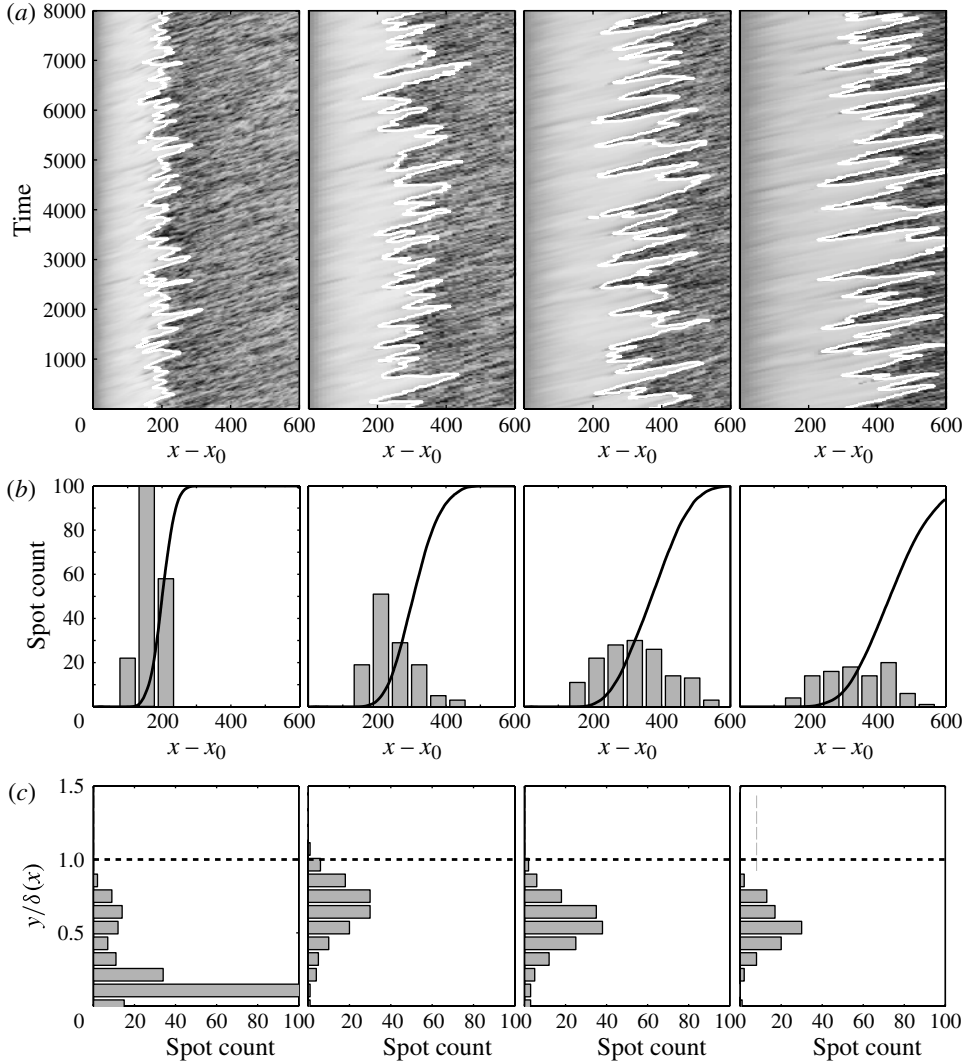


FIGURE 26. (a) Time–space diagrams showing the  $u'$  flow history for each case: adverse to favourable (left to right). The interface between the (light) laminar region and the (dark) turbulent region is marked in white. (b) Normalized distributions of streamwise spot-inception location for each case with intermittency distribution. (c) Distribution of wall-normal spot-inception locations for each case.

return level of 0.1, the lowest curve, the return period quickly drops from a high value at the inlet to order unity, signifying that streaks of this amplitude are ubiquitous. Similar behaviour follows for larger-amplitude streaks but with increasingly longer return periods.

It is evident from figure 27 that the highest frequency of spot inception is spatially correlated with the minimum return period for high-amplitude streaks. This result reaffirms the role of the highest-amplitude streaks in the bypass transition process – a role previously masked by time-averaged statistics (e.g.  $u_{rms}$ ).

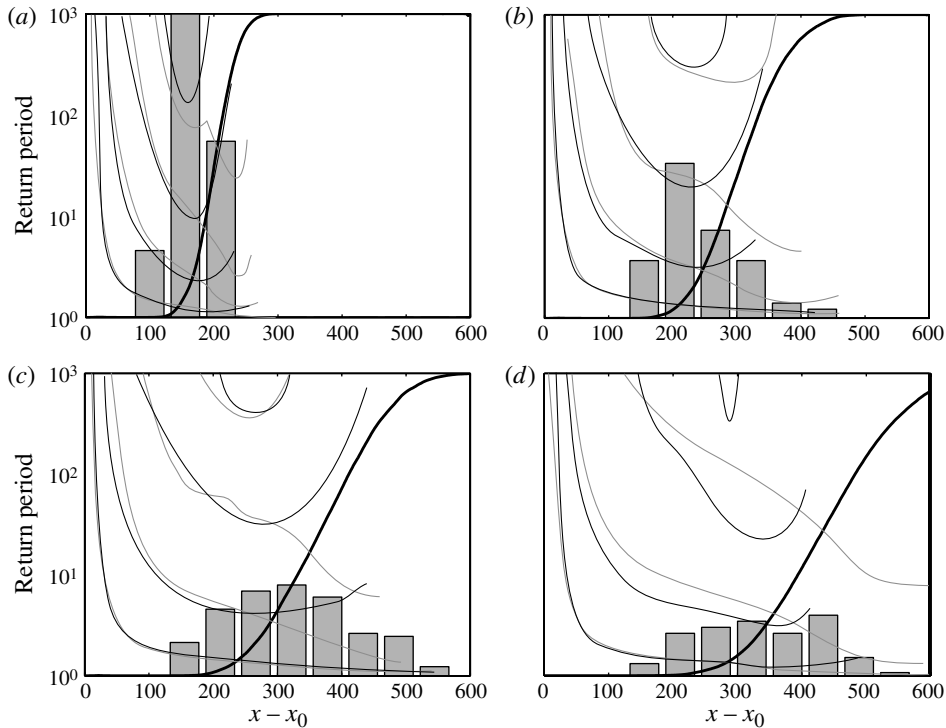


FIGURE 27. Histograms of spot inception rate versus streamwise location for all cases: (a)  $APG_{strong}$ , (b)  $APG$ , (c)  $ZPG$ , (d)  $FPG$ . Overlaid are contour lines of return level [0.1, 0.2, 0.3, 0.4] for positive (black) and negative (grey) streaks. Shown also is the intermittency distribution as in figure 26.

### 5.1. Turbulent spot growth

The conical growth of a single turbulent spot from the  $APG$  case is shown in figure 28. Outlines of the silhouette of the spot in each plane are shown for every 20th time unit. Figure 28(a) shows a side view of the spot evolution: the point of inception is near the free stream. In time, the spot fills the entire boundary-layer thickness, and extends from the wall to beyond the boundary-layer edge. At the later stages, an overhang develops at the leading edge of the spot. In figure 28(b), dotted lines mark the loci of conical growth, which has a spreading angle of  $12^\circ$ . It has been reported that adverse pressure gradient leads to wider spreading angles (Chong & Zhong 2005). This is also found in the current data with spreading angles from  $10^\circ$  to  $30^\circ$  with increasingly adverse pressure gradient. The dimensions and the volume of all observed turbulent spots were recorded. Figure 29 shows the time evolution of spot length and spanwise size for all pressure gradients and a linear fit of the data.

The growth rates in the streamwise and spanwise directions appear to have little dependence on pressure gradient. While there is some scatter in the data due to short-term erratic growth at spot extremities, all cases follow the same growth rate on average, and quickly return to this growth rate after any sudden changes such as the consumption of an additional streak breakdown adjacent to the spot.

Unlike the spreading angle, which is sensitive to the free stream velocity driving the spot convection, the spanwise size  $L_z$  and its growth rate are simply a measure of

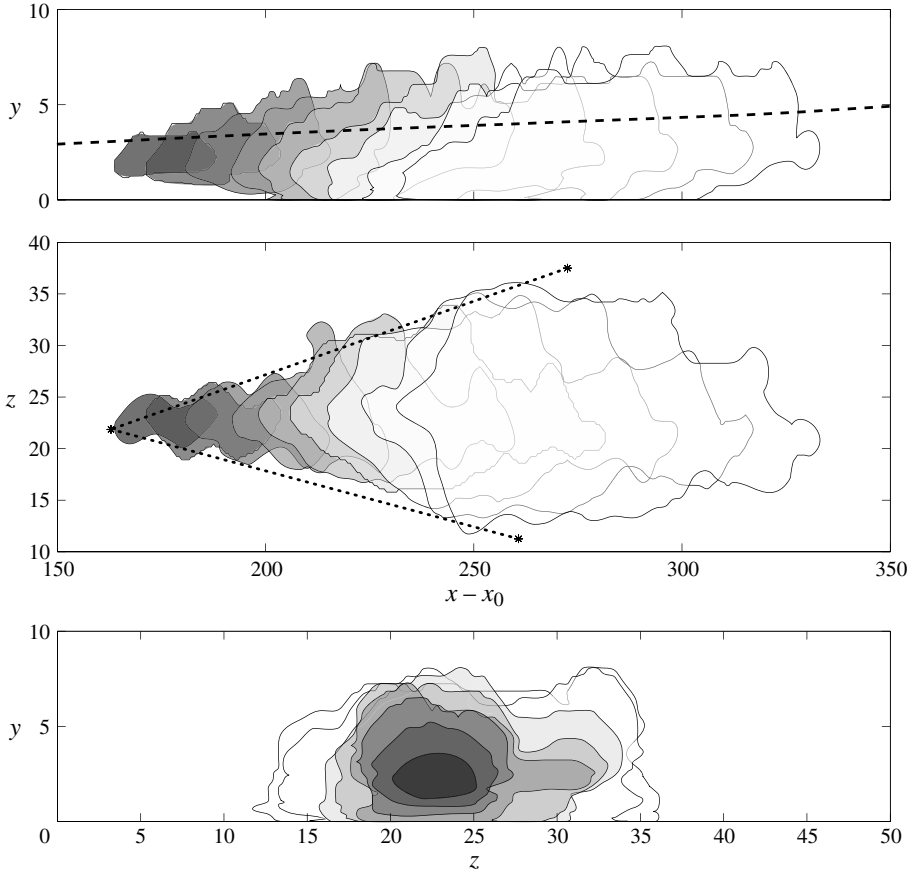


FIGURE 28. The history of the growth of a single spot from the *APG* case showing the extreme outline of the spot every 20th time unit. Shown are side, plan and front views, with the time-averaged laminar-conditioned boundary-layer thickness indicated by a dashed line.

the growth of the spot over time as it consumes surrounding laminar fluid. As can be seen in figure 29, this has a consistent linear behaviour for all cases,  $dL_z/dt \approx 0.11$ . Hence with favourable (adverse) pressure gradient, the spreading angle of the spot will decrease (increase) since the spot is swept downstream faster (slower) while its spreading rate is independent of the pressure gradient.

Similarly, spot length  $L_x$  grows at a rate of  $dL_x/dt \approx 0.46$ . The ratio of the spanwise and streamwise growth rates gives a propagation parameter  $\sigma = 0.24$  similar to that reported in the experimental literature (Mayle 1999). Spot area can then be expressed as a simple geometric growth,  $\text{area}(t) = 0.46 \times 0.11 \times t^2$ . This is shown in figure 30(a), and is in good agreement with the spot projected area onto the wall.

The time dependence of the spot volume is plotted in figure 30(b). A power-law fit with an exponent of 2.42 is fitted,  $\text{volume} \propto t^{2.42}$ . The greater than quadratic dependence on time can be accounted for by the wall-normal growth of the spot as shown in figure 31. The area and volumetric growth rates exhibit considerably less scatter than found for the spot size measurements in  $x$ ,  $y$  and  $z$ , since integral quantities are less sensitive to the instantaneous variation of the spot boundary. Most

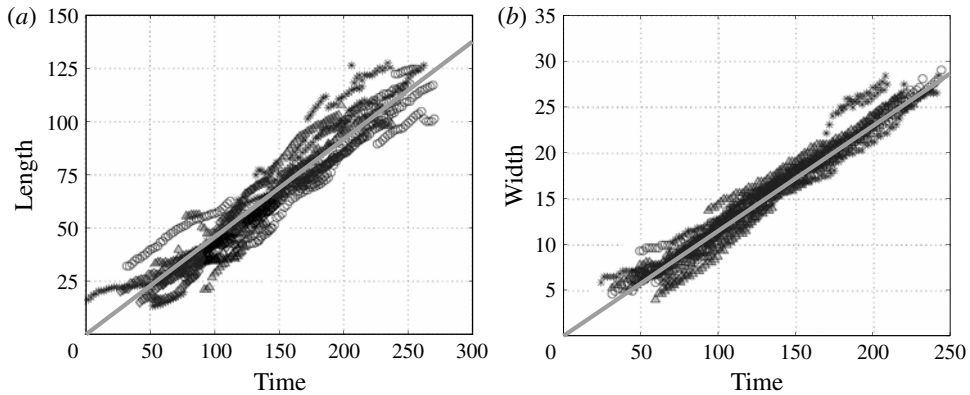


FIGURE 29. (a) Spot length and (b) width as functions of time for all cases:  $\circ$ , ZPG;  $*$ , FPG;  $\blacktriangle$ , APG;  $\diamond$ , APG<sub>strong</sub>. The slopes of the fitted lines are 0.46 and 0.11, respectively.

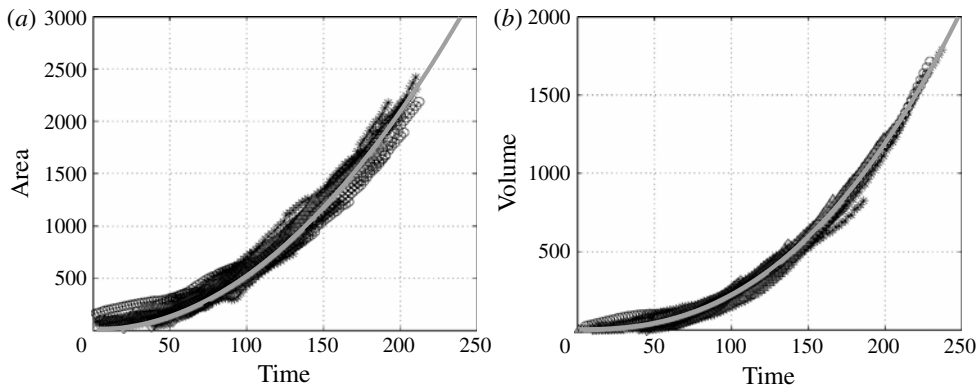


FIGURE 30. Maximum spot (a) footprint and (b) volume as functions of time for all cases. Also shown is the power law area =  $0.46 \times 0.11 \times t^2$  based on the geometric growth of the spot footprint, and a power-law fit with an exponent of 2.42 for the spot volume.

importantly, the current results illustrate that the spot growth rates are independent of pressure gradient – a valuable finding for transition modelling.

## 6. Discussion and conclusions

Conditional sampling of flow fields from DNS has yielded deeper insights into bypass transition. Whereas the time-averaged statistics show a smooth transition of the flow from a laminar to a fully turbulent state, the intermittency weighted statistics yield a distinctly different picture. With the exception of streamwise distortion due to streaks, the non-turbulent conditioned data retain laminar characteristics throughout the transition region. The turbulent-conditioned data reproduce a fully turbulent velocity profile, even from the onset of transition. The Reynolds stresses, however, initially exceed the level of a fully turbulent flow, but steadily decay towards these levels over the course of transition.

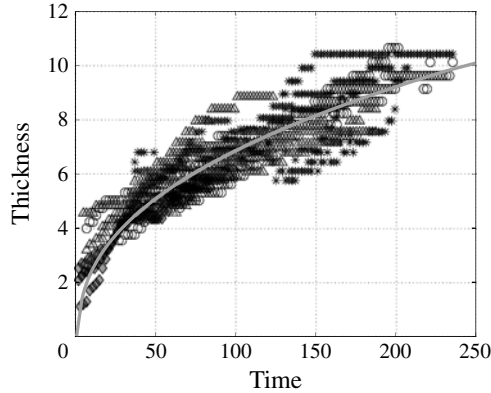


FIGURE 31. Spot thickness as a function of time for all cases. Also shown is a power-law fit with an exponent of 0.42. This indicates the wall-normal contribution to the volumetric growth.

Quadrant analysis confirms the significance of sweep and ejection events as the primary contributors to wall-normal momentum transfer. The turbulent-conditioned data identify ejections as the dominant event, being consistently 25% higher in magnitude than sweeps. Quadrant hole analysis provides an in-depth view of the contributions to the Reynolds shear stress. Similar findings to Nolan *et al.* (2010) are reported, with very large contributions due to ejection events resulting from short periods of time at the mean boundary-layer edge. Similar behaviour is found for sweep events near the wall.

By considering the role of individual streaks in the breakdown process, a better understanding of the seemingly random nature of turbulent spot formation is possible. In an attempt to understand why particular streaks undergo breakdown to turbulence, an algorithm for isolating streaks and extracting their amplitude was developed. The algorithm also tracks the spatial and temporal evolution of individual streaks. Therefore each streak becomes a single event in our statistical treatment. This is contrasted with simple time-averaging techniques where a streak is repeatedly sampled in space and time.

The streak amplitudes are demonstrated to adhere to a generalized extreme value distribution, which models local maxima of a dataset, and streak amplitudes fulfil this criterion. The distribution of streak amplitude shows that the most probable events are of the order of 10–15% of the local free stream velocity in the transition region (figure 23). However, the strongest streaks, which break down to turbulence, are less frequent and can reach amplitudes up to 30–40%. These streaks are more frequent with adverse pressure gradient (figure 25). The spot inception rate is also increased under these conditions (figure 26).

The location of spot inception and the subsequent growth rates of turbulent spots were reported. The wall-normal location of spot inception for the *FPG*, *ZPG* and *APG* cases is found to be distributed in the outer half of the boundary layer. This is in agreement with the observations of Jacobs & Durbin (2001). However, the *APG<sub>strong</sub>* case is different, where spot inception occurs close to the wall.

The streamwise locations of spot inception are clustered in the early stages of transition,  $0 < \gamma(x) < 0.5$ . Applying both the streak detection and laminar–turbulent discrimination algorithms, the streak amplitude at the point of spot inception is

generally found to exceed 20% of the local free stream velocity. The return level data show that streaks with amplitudes in excess of this threshold are frequent in this region (i.e. have short return period).

Turbulent spot growth rates were reported for all pressure gradients. Unlike the often cited spreading angle, which depends on the spot propagation rate, growth rates of streamwise and spanwise extent were found to be insensitive to pressure gradient. Consequently, the growth rate of the turbulent spot planform area for all spots grows quadratically in time. The volumetric growth rate follows a power law, volume  $\propto t^{2.42}$ , for the investigated range of mean pressure gradient.

## Acknowledgements

This work is supported by the European Commission Seventh Framework Programme under a Marie Curie Intra-European Fellowship. Further support was provided by the UK Engineering and Physical Sciences Research Council (EPSRC).

## REFERENCES

- ABU-GHANNAM, B. & SHAW, R. 1980 Natural transition of boundary layers – the effects of turbulence, pressure gradient, flow history. *J. Mech. Engng Sci.* **22**, 213–228.
- ANDERSSON, P., BERGGREN, M. & HENNINGSON, D. S. 1999 Optimal disturbances and bypass transition in boundary layers. *Phys. Fluids* **11** (1), 134–150.
- ANDERSSON, P., BRANDT, L., BOTTARO, A. & HENNINGSON, D. S. 2001 On the breakdown of boundary layer streaks. *J. Fluid Mech.* **428**, 29–60.
- ANTHONY, R., JONES, T. & LAGRAFF, J. 2005 High frequency surface heat flux imaging of bypass transition. *Trans. ASME: J. Turbomach.* **127**, 241–250.
- BRANDT, L., SCHLATTER, P. & HENNINGSON, D. S. 2004 Transition in boundary layers subject to free stream turbulence. *J. Fluid Mech.* **517**, 167–198.
- CANTWELL, B., COLES, D. & DIMOTAKIS, P. 1978 Structure and entrainment in the plane of symmetry of a turbulent spot. *J. Fluid Mech.* **87** (04), 641–672.
- CHING, C. Y. & LAGRAFF, J. E. 1995 Measurement of turbulent spot convection rates in a transitional boundary layer. *Exp. Therm. Fluid Sci.* **11** (1), 52–60.
- CHONG, T. P. & ZHONG, S. 2005 On the three-dimensional structure of turbulent spots. *Trans. ASME: J. Turbomach.* **127** (3), 545–551.
- COLES, S. 2001 *An Introduction to Statistical Modelling of Extreme Values*. Springer.
- DHAWAN, S. & NARASIMHA, R. 1958 Some properties of boundary layer flow during the transition from laminar to turbulent motion. *J. Fluid Mech.* **3** (04), 418–436.
- DURBIN, P. & WU, X. 2007 Transition beneath vortical disturbances. *Annu. Rev. Fluid Mech.* **39** (1), 107–128.
- EMMONS, H. W. 1951 The laminar–turbulent transition in a boundary layer. Part I. *J. Aero. Sci.* **18**, 490–498.
- GAD-EL-HAK, M., BLACKWELDERF, R. F. & RILEY, J. J. 1981 On the growth of turbulent regions in laminar boundary layers. *J. Fluid Mech.* **110**, 73–95.
- GOLDSTEIN, M. & WUNDROW, D. 1998 On the environmental realizability of algebraically growing disturbances and their relation to Klebanoff modes. *Theor. Comput. Fluid Dyn.* **10**, 171–186.
- HEDLEY, T. B. & KEFFER, J. F. 1974 Turbulent/non-turbulent decisions in an intermittent flow. *J. Fluid Mech.* **64** (04), 625–644.
- HERNON, D., WALSH, E. J. & MCELIGOT, D. M. 2007 Experimental investigation into the routes to bypass transition and the shear-sheltering phenomenon. *J. Fluid Mech.* **591**, 461–479.
- HULTGREN, L. S. & GUSTAVSSON, L. H. 1981 Algebraic growth of disturbances in a laminar boundary layer. *Phys. Fluids* **24** (6), 1000–1004.
- JACOBS, R. G. & DURBIN, P. A. 2001 Simulations of bypass transition. *J. Fluid Mech.* **428**, 185–212.

- KENDALL, J. 1991 Studies on laminar boundary-layer receptivity to free stream turbulence near a leading edge. In *Boundary Layer Stability and Transition to Turbulence* (ed. X. Reda *et al.*), ASME-FED, vol. 114. pp. 23–30.
- KLEBANOFF, P. 1971 Effect of free stream turbulence on the laminar boundary layer. *Bull. Am. Phys. Soc.* **10**, 1323.
- KLEISER, L. & ZANG, T. A. 1991 Numerical simulation of transition in wall-bounded shear flows. *Annu. Rev. Fluid Mech.* **23** (1), 495–537.
- LANDAHL, M. T. 1975 Wave breakdown and turbulence. *SIAM J. Appl. Maths* **28** (4), 735–756.
- LIN, J., LAVAL, J., FOUCAUT, J. & STANISLAS, M. 2008 Quantitative characterization of coherent structures in the buffer layer of near-wall turbulence. Part 1. Streaks. *Exp. Fluids* **45**, 999–1013.
- LIU, Y., ZAKI, T. A. & DURBIN, P. A. 2008a Boundary layer transition by interaction of discrete and continuous modes. *J. Fluid Mech.* **604**, 199–233.
- LIU, Y., ZAKI, T. A. & DURBIN, P. A. 2008b Floquet analysis of the interaction of Klebanoff streaks and Tollmien–Schlichting waves. *Phys. Fluids* **20**, 124192.
- MANS, J., KADIJK, E., LANGE, H. & STEENHOVEN, A. 2005 Breakdown in a boundary layer exposed to free stream turbulence. *Exp. Fluids* **39** (6), 1071–1083.
- MARQUILLIE, M., EHRENSTEIN, U. & LAVAL, J.-P. 2011 Instability of streaks in wall turbulence with adverse pressure gradient. *J. Fluid Mech.* **681**, 205–240.
- MATSUBARA, M. & ALFREDSSON, P. 2001 Disturbance growth in boundary layers subjected to free stream turbulence. *J. Fluid Mech.* **430**, 149–168.
- MAYLE, R. E. 1999 A theory for predicting the turbulent-spot production rate. *Trans. ASME: J. Turbomach.* **121** (3), 588–593.
- NAGARAJAN, S., LELE, S. K. & FERZIGER, J. H. 2007 Leading-edge effects in bypass transition. *J. Fluid Mech.* **572**, 471–504.
- NOLAN, K. P. & WALSH, E. J. 2012 Particle image velocimetry measurements of a transitional boundary layer under free stream turbulence. *J. Fluid Mech.* **702**, 215–238.
- NOLAN, K. P., WALSH, E. J. & MCELIGOT, D. M. 2010 Quadrant analysis of a transitional boundary layer subject to free stream turbulence. *J. Fluid Mech.* **658**, 310–335.
- OTSU, N. 1979 A threshold selection method from grey-level histograms. *IEEE Trans. Syst. Man Cybern.* **9** (1), 62–66.
- PARK, G. I., WALLACE, J. M., WU, X. & MOIN, P. 2012 Boundary layer turbulence in transitional and developed states. *Phys. Fluids* **24** (3), 035105.
- PHILLIPS, O. 1969 Shear-flow turbulence. *Annu. Rev. Fluid Mech.* **1**, 245–264.
- POPE, S. B. 2001 *Turbulent Flows*. Cambridge University Press.
- ROSENFELD, M., KWAK, D. & VINOKUR, M. 1991 A fractional step solution method for the unsteady incompressible Navier–Stokes equations in generalized coordinate systems. *J. Comput. Phys.* **94** (1), 102–137.
- SCHLATTER, P., ÖRLÜ, R., LI, Q., BRETHER, G., FRANSSON, J. H. M., JOHANSSON, A. V., ALFREDSSON, P. H. & HENNINGSON, D. S. 2009 Turbulent boundary layers up to  $Re_\theta = 2500$  studied through simulation and experiment. *Phys. Fluids* **21** (5), 051702.
- SCHRADER, L.-U., BRANDT, L. & ZAKI, T. A. 2011 Receptivity, instability and breakdown of Görtler flow. *J. Fluid Mech.* **682**, 362–396.
- SCHUBAUER, G. B. & KLEBANOFF, P. S. 1955 Contributions on the mechanics of boundary-layer transition. NACA Tech. Rep. 1289.
- SEIFERT, A. & WYGNANSKI, I. J. 1995 On turbulent spots in a laminar boundary layer subjected to a self-similar adverse pressure gradient. *J. Fluid Mech.* **296**, 185–209.
- SWEARINGEN, J. D. & BLACKWELDER, R. F. 1987 The growth and breakdown of streamwise vortices in the presence of a wall. *J. Fluid Mech.* **182**, 255–290.
- TAYLOR, G. I. 1923 Stability of a viscous liquid contained between two rotating cylinders. *Phil. Trans. R. Soc. Lond. A* **223**, 605–615.
- VAUGHAN, N. J. & ZAKI, T. A. 2011 Stability of zero-pressure-gradient boundary layer distorted by unsteady Klebanoff streaks. *J. Fluid Mech.* **681**, 116–153.

- VOLINO, R. J., SCHULTZ, M. P. & PRATT, C. M. 2003 Conditional sampling in a transitional boundary layer under high free stream turbulence conditions. *J. Fluids Engng* **125** (1), 28–37.
- WALLACE, J. M., ECKELMANN, H. & BRODKEY, R. S. 1972 The wall region in turbulent shear flow. *J. Fluid Mech.* **54** (1), 39–48.
- WILLMARTH, W. W. & LU, S. S. 1972 Structure of the Reynolds stress near the wall. *J. Fluid Mech.* **55** (1), 65–92.
- WU, X. & DURBIN, P. 2001 Evidence of longitudinal vortices evolved from distorted wakes in a turbine passage. *J. Fluid Mech.* **446**, 199–228.
- WUNDROW, D. & GOLDSTIEN, M. 2001 Effect on a laminar boundary layer of small amplitude streamwise vorticity in the upstream flow. *J. Fluid Mech.* **426**, 229–262.
- WYGNANSKI, I., SOKOLOV, M. & FRIEDMAN, D. 1976 On a turbulent ‘spot’ in a laminar boundary layer. *J. Fluid Mech.* **78** (4), 785–819.
- ZAKI, T. A. & DURBIN, P. A. 2005 Mode interaction and the bypass route to transition. *J. Fluid Mech.* **531**, 85–111.
- ZAKI, T. A. & DURBIN, P. A. 2006 Continuous mode transition and the effects of pressure gradient. *J. Fluid Mech.* **563**, 357–388.
- ZAKI, T. A., WISSINK, J. G., DURBIN, P. A. & RODI, W. 2009 Direct computations of boundary layers distorted by migrating wakes in compressor cascade. *Flow Turbul. Combust.* **83**, 307–322.
- ZAKI, T. A., WISSINK, J. G., RODI, W. & DURBIN, P. A. 2010 Direct numerical simulations of transition in a compressor cascade: the influence of free-stream turbulence. *J. Fluid Mech.* **665**, 57–98.